

RESEARCH ARTICLE SUMMARY

NEUROSCIENCE

Event structure sculpts neural population dynamics in the lateral entorhinal cortex

Benjamin R. Kanter*, Christine M. Lykken, Ignacio Polti, May-Britt Moser, Edvard I. Moser*



Full article and list of author affiliations: <https://doi.org/10.1126/science.adr0927>

INTRODUCTION: Our experience of the world unfolds as a stream of events that can later be reconstructed from memory in rich detail. The hippocampal formation, which is critical for such episodic memories, has been shown to exhibit slow changes in neural activity over time, most prominently in the lateral entorhinal cortex (LEC). It remains to be determined whether and how this drift in neural activity contributes to the temporal organization of episodic memories.

RATIONALE: Experiences are segmented into discrete events across a range of timescales from seconds to minutes or more. Event boundaries (i.e., transitions between successive events, such as changes in location, social setting, or behavior) affect memory for the duration and order of events, which suggests that event structure could play an important role in shaping the neural activity underlying such memories. To search for the neural mechanisms that determine how events are segmented and organized in time, we used high-density Neuropixels probes to record neural activity from an unprecedented number of neurons in the LEC and neighboring brain areas in freely behaving rats, across multiple behaviors and behavioral states, and in the presence of variations in event structure at multiple timescales.

RESULTS: Neural population activity in the LEC drifted continuously along a one-dimensional manifold during individual foraging sessions, such that activity traveled progressively farther away from the current state. Simultaneously recorded neural activity in the medial entorhinal cortex (MEC) and hippocampal area CA1 exhibited minimal drift. Recordings during natural sleep revealed that LEC population dynamics were nearly identical during rapid eye movement (REM) sleep and foraging, which suggests that drift does not require changes in external sensory information and instead is an inherent network phenomenon. During wakefulness, population

dynamics abruptly shifted at event boundaries, leading to the segmentation of neural activity into discrete temporal units. During tasks with repeating temporal structure, the LEC simultaneously encoded event information across multiple timescales by traveling additionally in directions orthogonal to the drift. We uncovered potential mechanisms of both drifting and shifting dynamics in neural population activity. Drift could be explained by minute-scale variability in the firing rate of individual neurons broadly distributed throughout the LEC population. These slow variations were necessary and sufficient for drift at the population level. Shifts in population dynamics at event boundaries were driven by synchronous responses of neural ensembles in the LEC. Different ensembles responded at different event boundaries, such that individual events could be time-stamped in memory.

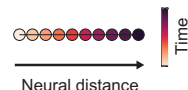
CONCLUSION: Drift of neural activity in the LEC is an inherent network phenomenon that continues at a constant rate during wakefulness and sleep but is briefly interrupted by abrupt shifts at moments of transition between events. These results identify a candidate mechanism for the segmentation of experience into discrete episodic memories, as reported in human study participants. Experience consists of a sequence of events across a wide range of timescales, organized hierarchically from seconds to minutes or more. We show that LEC activity simultaneously encodes event information across these different timescales without explicit reinforcement or extensive behavioral training. Together, our results identify a hierarchical neural coding scheme for organizing events in time. □

*Corresponding author. Email: benjamin.kanter@ntnu.no (B.R.K.); edvard.moser@ntnu.no (E.I.M.) Cite this article as B. R. Kanter *et al.*, *Science* **388**, eadr0927 (2025). DOI: 10.1126/science.adr0927

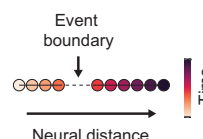
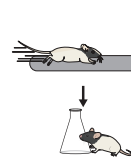
Neural population activity in the LEC organizes events in time.

Activity inherently drifts over time regardless of behavioral state (left). In the awake state, activity abruptly shifts to segment events (middle). Activity travels in additional directions orthogonal to the drift to simultaneously encode event information across multiple timescales (right). The LEC uses a hierarchical coding scheme for organizing events in time. [Art adapted from SciDraw (scidraw.io), CC-BY 4.0]

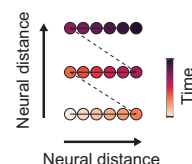
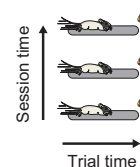
LEC population activity drifts in all behavioral states



LEC dynamics abruptly shift to segment events



LEC encodes event information across timescales



NEUROSCIENCE

Event structure sculpts neural population dynamics in the lateral entorhinal cortex

Benjamin R. Kanter*, Christine M. Lykken, Ignacio Polti, May-Britt Moser, Edvard I. Moser*

Our experience of the world is a continuous stream of events that must be segmented and organized at multiple timescales. The neural mechanisms underlying this process remain unknown. In this work, we simultaneously recorded hundreds to thousands of neurons in the lateral entorhinal cortex of freely behaving rats. Neural population activity drifted continuously along a one-dimensional manifold during all behaviors and behavioral states, including sleep, which points to an intrinsic origin of the drift. In awake animals, boundaries between events were associated with discrete shifts in population dynamics, which segmented the neural activity into temporal units. During tasks with recurring temporal structure, activity traveled additionally in directions orthogonal to the drift, encoding event information across multiple timescales. The results identify a hierarchical coding scheme for organizing events in time.

We experience the world as a continuous stream of events (1) occurring in a particular order at particular places and times. Episodic memory allows us to mentally revisit those experiences by recalling events in sequence (2). Although the hippocampus is critical for episodic memory (3, 4) and the spatial correlates of such memories have been well described (5, 6), much less is known about the neural mechanisms underlying their temporal organization (7). The passage of time is mirrored by slow drift in neural activity in the hippocampus (8–12) and one of its major cortical inputs, the lateral entorhinal cortex (LEC) (13, 14), but the contribution of this drift to the temporal organization of episodic memories has not been determined. It remains unknown whether the drift of neural population activity is steady and continuous in time, whether it is determined by intrinsic network dynamics or reflects the structure of experience, and whether and how experience is simultaneously encoded at multiple timescales (15, 16).

One important clue is that experience is hierarchically segmented into discrete events across timescales from seconds to minutes or more (17). Event boundaries (i.e., transitions between successive events) are associated with abrupt changes in behavior, the environment, or physical location. Such boundaries affect memory for the duration and order of events (10, 17–21) and are accompanied by transient changes in hippocampal activity (10, 16, 21–24). To search for the neural mechanisms that determine how events are segmented and organized in time, we monitored the activity of large populations of neurons in rats during single episodes of experience. We focused on brain areas where neural activity is correlated with the passage of time (8, 9, 12, 13). We used high-density Neuropixels 2.0 silicon probes (25) to perform simultaneous extracellular recordings of >1000 neurons in the LEC, medial entorhinal cortex (MEC), and hippocampal area CA1 of freely behaving rats across multiple behaviors and behavioral states and in the presence of variations in event structure at multiple timescales.

Large-scale recordings show continuous drift in LEC population activity

To address whether drift in neural population activity in the LEC is continuous in time and how both intrinsic factors and the structure of the animal's experience may shape those dynamics, we decided to first verify that the drift previously observed in data pooled across sessions and animals (13) is also expressed during individual events. To quantify population dynamics without averaging data over events, we used high-density Neuropixels silicon probes, which increased the yield of recorded neurons by an order of magnitude (Fig. 1A; mean single session yield across 9 rats = 772 LEC neurons; tables S1 and S2 and figs. S1 to S3). Neural activity was recorded while rats engaged in a free foraging task (Materials and methods). We temporally binned the spiking activity of each LEC neuron to capture dynamics at the behavioral timescale of seconds to minutes (bin size = 10 s). To visualize the neural population dynamics as trajectories through a state space of neural activity, we used dimensionality reduction [principal components analysis (PCA) and linear discriminant analysis (LDA)] (figs. S4 and S5 and Materials and methods). Population activity in the LEC drifted over the course of minutes like an “arrow of time,” such that the activity at any given time was most similar to the neighboring time points and became progressively more dissimilar over time (Fig. 1B, left, and figs. S5 and S6). There was little drift in the MEC and CA1 during the exact same experience (Fig. 1B, middle and right, and figs. S5 and S6). Note that we use the term drift as a description of the phenomenon, irrespective of any potential function.

Dimensionality reduction can cause distortions and be misleading when analysis is restricted to a specific projection of the data (26, 27). All of our analyses were therefore performed in the high-dimensional ambient space defined by the number of simultaneously recorded neurons, unless explicitly stated otherwise. To quantify the drift in population activity, we calculated the distance traveled (cosine distance ranging from 0 to 1) between all pairs of population vectors during the 10-min foraging session (Fig. 1C and fig. S5E). Distances in the LEC grew continuously as a function of the temporal lag between states, and activity drifted significantly farther over the course of the session in the LEC compared with the MEC and CA1 (Fig. 1, B to E, and fig. S6, A to D). Quantification of distance traveled was insensitive to the number of neurons sampled, and distances were consistently larger in the LEC compared with the MEC and CA1 in size-matched populations (fig. S6B). The regional differences were insensitive to the choice of temporal bin size (fig. S6C) or differences in the population firing rate changes between regions (fig. S4F). We also attempted to decode time within the foraging session based on activity from either the LEC, MEC, or CA1. We found that a k -nearest neighbors classifier ($k = 10$) was sufficient to decode time from LEC activity (ambient space) with significantly greater accuracy compared with the MEC and CA1 (Fig. 1F and fig. S6E; accuracy in all regions was above chance levels).

Drift of population activity is an inherent property of the LEC

Having established that LEC population activity drifts in the absence of scheduled events, we next investigated whether drift is propelled by changes in sensory inputs and behavior or is an inherent property of the LEC that persists regardless of these factors. To minimize the contribution of external sensory inputs and behavior, we recorded neural activity during natural sleep (Fig. 2A). Behavioral and neural data were used to segment sleep sessions post hoc into slow-wave sleep (SWS) and rapid eye movement (REM) sleep (Fig. 2B; fig. S7, A and B; and Materials and methods). Because SWS was dominated by frequent transitions between nearly silent DOWN states and short UP states (a few seconds or less; Fig. 2C and fig. S7C), we focused our analysis of drift instead on REM, where neural dynamics were continuous and exhibited firing rate characteristics more closely resembling wakefulness (Fig. 2C and fig. S7D). We focused on longer REM segments with more potential to exhibit drift (>60 s) and matched these segments

Kavli Institute for Systems Neuroscience and Centre for Algorithms in the Cortex, Norwegian University of Science and Technology, Trondheim, Norway. *Corresponding author. Email: benjamin.kanter@ntnu.no (B.R.K.); edvard.moser@ntnu.no (E.I.M.)

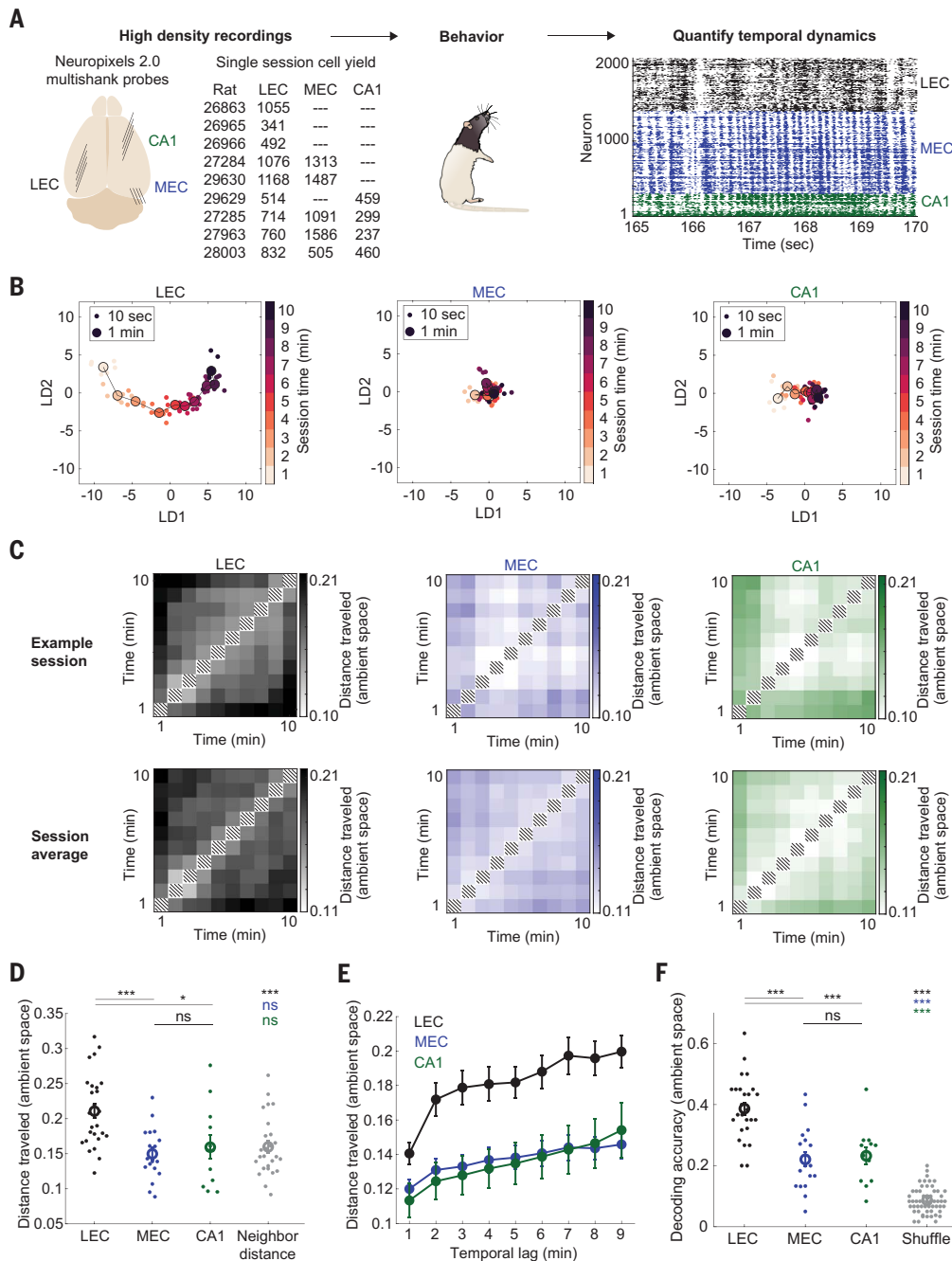


Fig. 1. Large-scale recordings show continuous drift in LEC population activity. (A) Summary of experimental approach. Neuropixels 2.0 silicon probes were used to record large populations of neurons simultaneously in one to three brain areas. Rats performed behavioral tasks with different degrees of event structure. Population dynamics were quantified during individual experiences. [Art adapted from SciDraw (scidraw.io), CC-BY 4.0] (B) Visualization of neural trajectories (from rat 27285) during 10-min foraging session shows population drift in the LEC (left) that is largely absent in simultaneously recorded MEC (middle) and CA1 (right) populations. State space is defined by top two linear discriminants LD1 and LD2 using 1-min epochs as class labels (Materials and methods). Small dots represent 10-s time bins, and large dots represent average activity during 1-min epochs. Points are colored from light to dark to show time within the session. (C) Matrices showing distance traveled (ambient space) throughout the 10-min foraging session for all brain areas in an example session [top row; corresponding to trajectories in (B)] and averaged over all sessions (bottom row; $n = 26, 18,$ and 12 sessions for LEC, MEC, and CA1, respectively). Hatched lines along main diagonal indicate that within-epoch distances were excluded to avoid saturating the color scale and focus on between-epoch distances. (D) Distance traveled (ambient space) between first and last minutes for all sessions and all areas. Neighbor distances compare adjacent times in the LEC as a lower bound of distance traveled. LEC versus MEC: $t(42) = 4.24; P = 1.19 \times 10^{-4}$. LEC versus CA1: $t(36) = 2.72; P = 0.01$. MEC versus CA1: $t(28) = -0.55; P = 0.59$. LEC versus neighbor: $t(50) = 3.86; P = 3.25 \times 10^{-4}$. MEC versus neighbor: $t(42) = -0.81; P = 0.43$. CA1 versus neighbor: $t(36) = -0.03; P = 0.98$. Two-sample t test; $n = 26, 18,$ and 12 sessions for LEC, MEC, and CA1, respectively. (E) Distance traveled (ambient space) as a function of temporal lag within the session for all sessions and all areas. Interaction effect between area and time: $F(16, 424) = 4.2; P = 1.39 \times 10^{-7}$, repeated measures analysis of variance (ANOVA). (F) Decoding accuracy for 1-min epochs within the session using a k -nearest neighbors classifier (ambient space). LEC versus MEC: $t(42) = 5.31; P = 3.83 \times 10^{-6}$. LEC versus CA1: $t(36) = 4.41; P = 9.02 \times 10^{-5}$. MEC versus CA1: $t(28) = -0.32; P = 0.75$. LEC versus shuffle: $t(80) = 18.87; P = 3.37 \times 10^{-31}$. MEC versus shuffle: $t(72) = 8.00; P = 1.55 \times 10^{-11}$. CA1 versus shuffle: $t(66) = 8.30; P = 7.65 \times 10^{-12}$. Two-sample t test; $n = 26, 18,$ and 12 sessions for LEC, MEC, and CA1, respectively. [(D) to (F)] Data are represented as individual foraging sessions and means \pm SEMs. *** $P < 0.001$; * $P < 0.05$; ns, not significant.

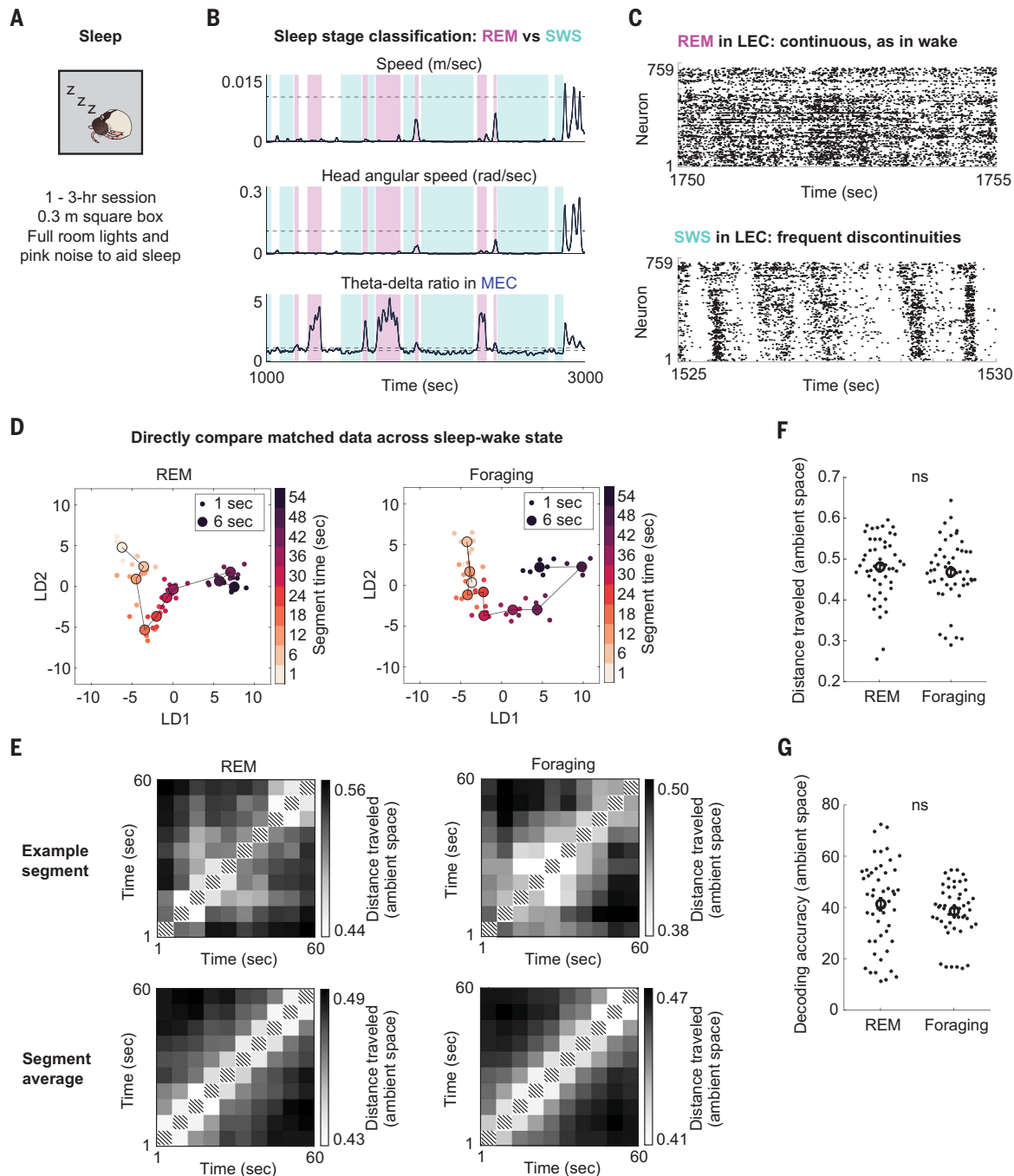


Fig. 2. Drift of population activity is an inherent property of the LEC. (A) Animals slept in a specially designed sleep box for several hours. [Art adapted from SciDraw (scidraw.io), CC-BY 4.0] (B) Data were classified as REM or SWS based on the theta/delta ratio recorded on a probe in the MEC or CA1 (47) but not in the LEC, where theta is notably absent. Plots show time courses of three variables used for detecting REM and SWS (thresholds depicted with gray dashed lines) for an example 30-min sleep interval (from rat 29630; see fig. S7A for all animals). (Top) Running speed. (Middle) Head angular speed. (Bottom) Theta (5 to 10 Hz)/delta (1 to 4 Hz) ratio from local field potential. (C) Raster plots of LEC activity from example segments of REM (top) and SWS (bottom) from sleep session shown in (B). Note the presence of continuous activity during REM (as in wake; Fig. 1A and fig. S7D) compared with the frequent discontinuities in SWS owing to transitions between active UP states and silent DOWN states (fig. S7C). (D) Visualization of neural trajectories (from rat 29630) show LEC population drift during a 60-s REM segment (left) that is comparable to a matched 60-s foraging segment (right). Small dots represent 1-s time bins, and large dots represent average activity during 6-s epochs. Points are colored from light to dark to show time within the segment. (E) Matrices showing mean distance traveled (ambient space) throughout an example (top row) 60-s segment of REM (left) or foraging (right) over all segments (bottom row) for each state in the LEC. Example matrices in the top row correspond to trajectories in (D). Note the similar patterns of drift between states. Hatching as in Fig. 1C. (F) Summary data showing distance traveled (ambient space) in the LEC during each 60-s REM segment for all sleep sessions was not different from matched 60-s foraging segments from the same animals. REM versus foraging: $U = 2681.00$; $P = 0.28$, Wilcoxon rank-sum test; $n = 50$ segments. (G) Summary data showing decoding accuracy (ambient space) in the LEC for each 60-s REM segment for all sleep sessions was not different from matched 60-s foraging segments from the same animals. REM versus foraging: $U = 2698.50$; $P = 0.23$, Wilcoxon rank-sum test; $n = 50$ segments. [(F) and (G)] Dots represent individual 60-s segments. Data are represented as means \pm SEMs. $***P < 0.001$; ns, not significant. Assumptions of parametric tests (i.e., normality, homogeneity of variance) were formally tested. When these assumptions were violated, alternative nonparametric tests or bootstrap resampling were used instead (Materials and methods).

to equivalent periods in the wake state to directly quantify the similarity between drift in REM sleep and foraging (fig. S7E and Materials and methods).

Neural trajectories in the LEC appeared similar during REM sleep and foraging, continuously evolving over time in both states (Fig. 2D). We quantified the drift in neural population activity by calculating the distance traveled (ambient space) between all time points during the 60-s segments (Fig. 2E). Activity drifted progressively farther away from the current state at each time point regardless of behavioral state. The total distance traveled (ambient space) from beginning to end of each 60-s segment was not significantly different in REM compared with foraging (Fig. 2F and fig. S7F). Cumulative distance traveled increased progressively during segments of both REM and foraging, with

no difference between them (fig. S7G). Decoding accuracy (ambient space) of time within each REM segment was as high as that during foraging (Fig. 2G). Drift was also observed to some extent in the CA1 and MEC during REM sleep (fig. S8).

Shifts in state space at event boundaries discretize experience

We next asked whether and how event boundaries modulate the inherently generated drift. LEC neurons are known to encode stimuli, such as odors and objects, through time-locked changes in firing rate (28–30). At the population level, such abrupt changes in firing rate could evoke abrupt shifts in the state space of neural activity, which would be detectable as brief moments of acceleration then deceleration of the neural trajectory (Fig. 3A). This would provide a simple

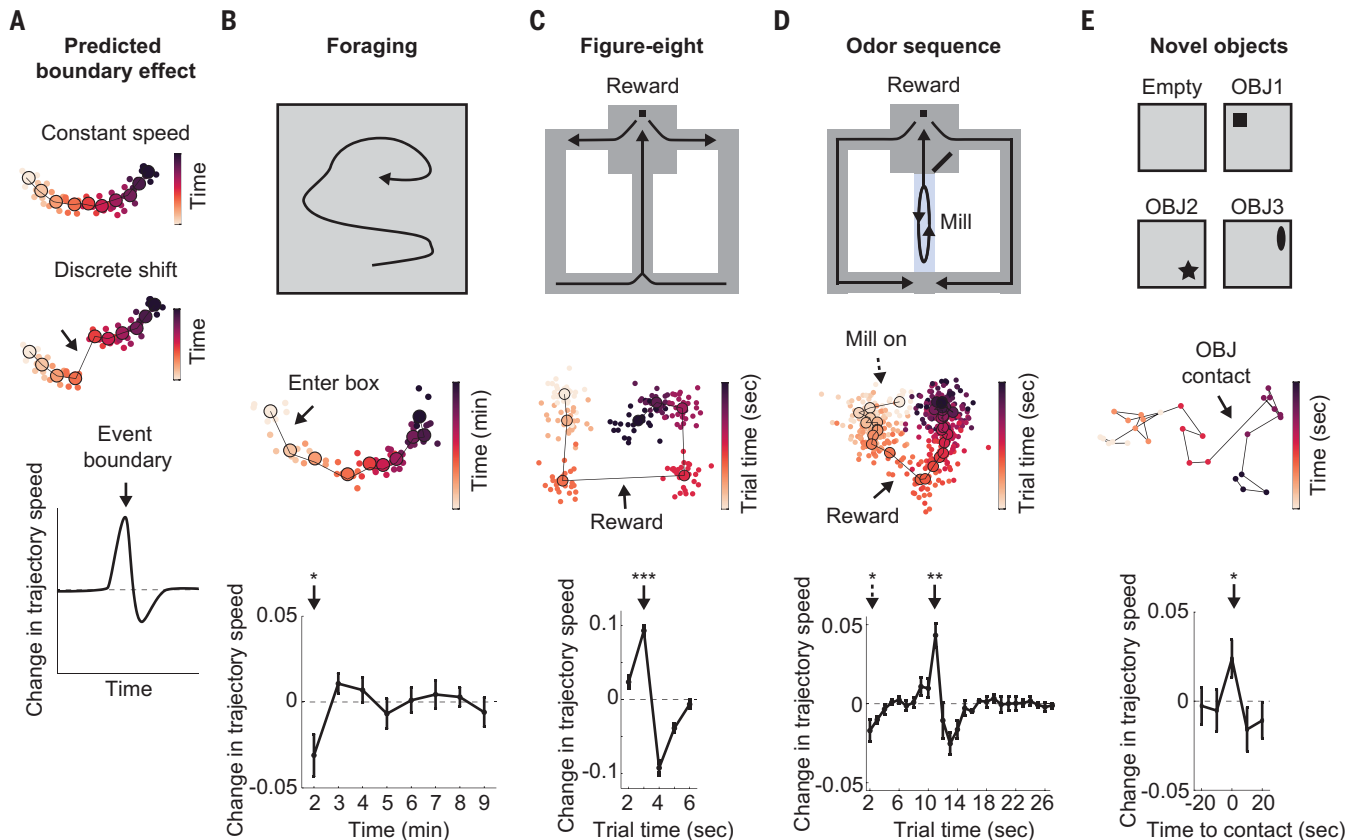


Fig. 3. Shifts in state space at event boundaries discretize experience. (A) Schematic illustrating the hypothesis that trajectories evolve at a constant speed within an event (top) and undergo discrete shifts at event boundaries (middle). Plotting the change in trajectory speed over time reveals a rapid acceleration then deceleration at the event boundary (bottom). (B) In the foraging task, entering the box was the only scheduled event boundary (top). Neural trajectories in the LEC decelerated after entering the box and then returned to a constant speed. Example trajectory (middle) with arrow indicating change in speed. Small dots represent 10-s time bins, and large dots represent average activity during 1-min epochs. Points are colored from light to dark to show time within the session. Mean change in trajectory speed (bottom) at each time point over all sessions with significant speed change at marked time point: $W = 45.00$; $P = 9.18 \times 10^{-4}$, Wilcoxon signed-rank test; $n = 26$ sessions. (C) In the figure-eight task, the reward on each trial (lap) was the only scheduled event boundary. Neural trajectories accelerated in the LEC during reward approach and then decelerated again on each trial. Data are displayed as in (B). Small dots represent 1-s time bins on each trial, and large dots represent average activity for that time bin over all trials. Points are colored from light to dark to show time within the trial. $t(4) = 21.11$; $P = 2.98 \times 10^{-5}$, one-sample t test; $n = 5$ sessions. (D) In the odor sequence task, there were two scheduled event boundaries per trial. Neural trajectories in the LEC decelerated after the treadmill turned on to start the trial. Neural trajectories accelerated in the LEC during reward approach and then decelerated again. Data are displayed as in (B). Small dots represent 1-s time bins on each trial, and large dots represent average activity for that time bin over all trials. Points are colored from light to dark to show time within the trial. Dashed arrow: $t(4) = -3.09$; $P = 0.037$. Solid arrow: $t(4) = 5.39$; $P = 0.006$, one-sample t test; $n = 5$ sessions. (E) In the novel objects task, the object explorations defined the event boundaries. Neural trajectories accelerated in the LEC at the first contact with each object. Data are displayed as in (B). Small dots represent 10-s time bins, and large dots represent average activity during 1-min epochs. Points are colored from light to dark to show time surrounding the first contact. $t(22) = 2.22$; $P = 0.037$, one-sample t test; $n = 23$ first contacts. [(B) to (E)] Similar results were obtained when down-sampling the population to have the same number of neurons across all brain areas (fig. S10): Foraging: $W = 43.00$; $P = 7.65 \times 10^{-4}$, Wilcoxon signed-rank test; $n = 26$ sessions. Odor sequence, dashed arrow: $t(4) = -3.35$; $P = 0.029$, one-sample t test; $n = 5$ sessions. Odor sequence, solid arrow: $t(4) = 5.42$; $P = 0.006$, one-sample t test; $n = 5$ sessions. Novel objects: $t(22) = 2.10$; $P = 0.047$, one-sample t test; $n = 23$ first contacts. Data are represented as means \pm SEMs. Change in trajectory speed was calculated as the difference between cosine distance (ambient space) for neighboring time points and the previous two neighboring time points. Statistical tests compare the time point, indicated with a black arrow, with a zero-mean null distribution. *** $P < 0.001$; ** $P < 0.01$; * $P < 0.05$.

mechanism for ensembles of coactive neurons to time-stamp event boundaries as the sequence of events is encoded into memory.

We searched for signatures of event segmentation in the LEC by measuring the acceleration profiles of neural trajectories in tasks containing different types of events over multiple timescales. In the foraging task described above, there were no scheduled event boundaries except for the introduction of the animal to the arena (animals could not predict when the session would end because sessions were of variable duration and truncated post hoc to 10 min for analysis purposes) (Fig. 3B). We found a deceleration of the trajectory during the first minutes of the session, consistent with a postboundary deceleration to baseline speed. Next, rats were trained to run self-paced laps around a figure-eight maze, motivated by a single reward at a constant location on each lap (Fig. 3C). Neural trajectories accelerated on each lap immediately before the animal reached the reward, which was the one scheduled event boundary in the task, and then decelerated again. Finally, we used an odor sequence task (Fig. 3D) that was quite similar to the figure-eight task. The only relevant difference here is that the central stem of the maze was a treadmill where the rat ran in place for 10 s, thus creating an additional event boundary within each trial (other task features are described below). We observed multiple changes in trajectory acceleration aligned to the multiple event boundaries within each trial of this task: a deceleration after the treadmill turned on, an acceleration during reward approach, and a deceleration when reaching the reward. Note how stable the trajectory speeds were within each event compared with the boundary-induced shifts.

To test whether the LEC is also sensitive to novel event boundaries, before learning, we scheduled event boundaries at times when neural trajectory speeds were known to be stable. Animals started by randomly foraging in an empty arena, as above, but every 7.5 min, an object that the animal had never seen before (a so-called novel object) was inserted at a pseudorandom location (Fig. 3E, top). We predicted that object exploration would elicit shifts in LEC activity owing to the coincident activation of object-responsive neurons (28, 29). Indeed, times of object exploration caused higher firing rates in LEC neurons compared with a size-matched population of other time points during the same session [$t(147) = 5.60$; $P = 1.04 \times 10^{-7}$, paired Student's t test; $n = 148$ time points]. Notably, the first exploration of each object was associated with acceleration of the neural trajectory at the time of contact with the object (Fig. 3E), similar to the familiar event boundaries in the other tasks. Subsequent exploration of the same objects did not cause shifts (fig. S9A).

To avoid biasing our search for shifts to periods of object exploration, we also performed an agnostic search of the whole experiment for any times where the network became suddenly active as putative times for shifts (Materials and methods). These onsets of synchronous activity were consistently associated with trajectory acceleration (fig. S9B). A large and significant fraction of these synchronous spike events corresponded to moments of object exploration ($33 \pm 8\%$; $n = 23$ objects; Fisher's exact test, $P = 0.002$). Similar results were obtained for agnostic searches across the trial-based tasks (figure-eight task: $62 \pm 8\%$ near reward location; $n = 5$ sessions; Fisher's exact test, $P = 1.14 \times 10^{-6}$; odor sequence task: $81 \pm 4\%$ near reward locations or treadmill start; $n = 10$ sessions; Fisher's exact test, $P = 0.36$, not significant due to animal spending 83% of time at these locations).

Event boundaries often coincide with changes in movement or arousal. The fact that later exploration of objects did not cause the same boundary-induced changes in neural activity as the first contacts (fig. S9A) suggests that such effects were likely not merely a result of changes in the animal's movement. To further exclude this possibility, we performed three additional controls. First, when considering every time point in each session, there was no systematic relationship between changes in animal speed and changes in neural trajectory speed in any task (fig. S9C). Second, in the foraging and novel objects tasks, where changes in movement could vary independently of the task structure, we found no significant change in animal speed at the event

boundaries (fig. S9D). Third, in the figure-eight and odor sequence tasks, where changes in movement were more rigidly controlled by the task structure, we found no evidence of trial-to-trial correlations between changes in animal speed and changes in neural trajectory speed at the event boundaries (fig. S9E). Instead, we observed acceleration of neural trajectories at event boundaries across a wide range of changes in running speed.

The observed dynamics are harder to dissociate from general arousal because event boundaries, by definition, draw the animal's attention and will therefore be accompanied by activation of widely projecting neuromodulatory systems in the brainstem. Nevertheless, if changes in trajectory speed were caused exclusively by changes in the activity of such systems, the effects would likely not be specific to the LEC. We therefore repeated the analyses on MEC and CA1 data and found that although these regions exhibited changes in trajectory speed in some conditions (fig. S10), only in the LEC was the effect robust across all tasks. The regional differences were not due to the number of neurons sampled (see legends of Fig. 3 and fig. S10).

Multiple timescales are encoded through orthogonal coding dimensions

Event memories are structured at multiple timescales, from seconds to minutes or hours. We thus asked whether different timescales could be encoded simultaneously in the LEC. The trial-based tasks described above contain a hierarchy of timescales, with individual laps occurring over seconds and the behavioral session occurring over minutes. To determine whether the LEC contains representations matching each of these timescales during ongoing behavior, we trained rats in a repetitive lap-running task that causes repetitive neural trajectories in the LEC (13) (Fig. 4A and fig. S11, A and B). From the continuous behavior in this task, we extracted 6-s trials (fig. S11, A to C) leading up to the reward (i.e., not including the reward-induced event boundary shown in Fig. 3C). LEC activity followed similar trajectories during these 6 s on each lap (trial time; Fig. 4, B and E, and fig. S11, D, F to I, and L). The large population recordings enabled us to analyze individual trials and compare the trajectories lap-by-lap. We directly quantified alignment of the trajectories across trials by comparing distances (ambient space) between matched trial times (i.e., the same 1-s time bin across different trials) with distances between mismatched trial times. Distances between matched trial times were significantly smaller (Fig. 4C), which indicates that trajectories from different trials were aligned. Alignments were maintained between trajectories for different trial types (left- versus right-turn trials) (fig. S11I). We further confirmed that activity repeated across trials by accurately decoding trial time (ambient space) from held-out trials using a k -nearest neighbors classifier (Fig. 4D).

This finding of repeating trajectories during repetitive behavior is quite the opposite of continuous drift. Thus, to determine whether the repetitive nature of the task also affected dynamics at slower timescales, we zoomed out to the timescale of the behavioral session and asked whether drift over minutes was preserved. We performed the exact same analysis as in the foraging task to capture change over minutes while ignoring the lap-running behavior. Continuous drift was still observed (Fig. 4F and fig. S11, E and J to L) during the exact same behavioral session while repeating trajectories occurred at a faster timescale (Fig. 4E and fig. S11L). This suggests that drift and repeating trajectories toward learned event boundaries may evolve along independent dimensions in the state space of neural activity and that information about these two timescales is mixed within the activity of the same neural population (fig. S11, L to O).

To quantify whether neural activity traveled in orthogonal directions at these two timescales (trial time versus session time), we identified the coding dimensions separately using PCA/LDA (PCA followed by LDA). For each timescale, the analyses yielded a vector describing the dynamics of the exact same population of neurons. The angle between

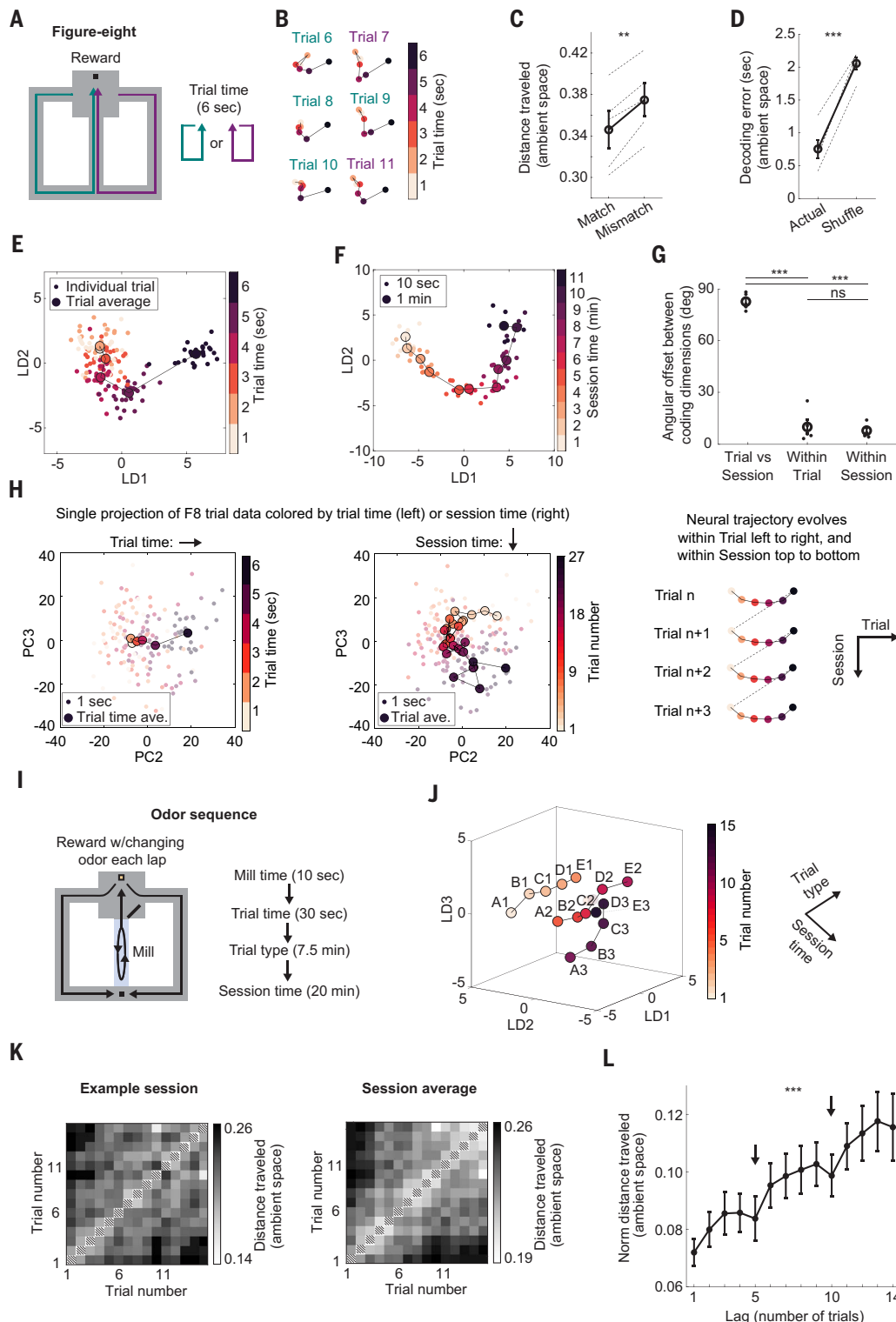


Fig. 4. Diverse timescales are encoded in LEC activity using orthogonal coding dimensions. (A) In the figure-eight task, rats were trained to run self-paced laps to receive milk rewards at the top of the maze, returning down the arm of their choice. Trial times were defined post hoc as 6 s leading up to but excluding the reward. (B) Example neural trajectories in the LEC from light to dark points during individual trials show that these trajectories were aligned across trials. (C) At each trial time, distances (ambient space) in the LEC between matched trial times from other trials were smaller compared with mismatched times from other trials. Match versus mismatch: $t(4) = 6.94$; $P = 0.002$, paired t test; $n = 5$ sessions. (D) Decoding accuracy (ambient space) in the LEC for 1-s trial times using a k -nearest neighbors classifier trained on held-out trials. Actual versus shuffle: $t(4) = -12.38$; $P = 2.45 \times 10^{-4}$, paired t test; $n = 5$ sessions. (E) Trial-averaged neural trajectory for example session in the LEC, where small dots represent 1-s time bins on each trial, and large dots represent average activity for that time bin over all trials. Points are colored from light to dark to show time within the trial. (F) Ignoring trial structure and looking for drift as in the foraging task shows that repeating neural trajectories across trials in the LEC did not eliminate drift over the course of the session. Small dots represent 10-s time bins, and large dots represent average activity for 1-min epochs. Points are colored from light to dark to show time within the session. (G) The axes of travel during each trial versus during the entire session were approximately orthogonal. “Trial versus session” versus “within trial”: $t(4) = 13.66$; $P = 1.66 \times 10^{-4}$. “Trial

versus session" versus "within session": $t(4) = 20.29$; $P = 3.48 \times 10^{-5}$. "Within trial" versus "within session": $t(4) = 0.51$; $P = 0.63$. Paired t test; $n = 5$ sessions. (H) Same example session from (E) and (F) showing a single projection of trial data in the subspace defined by PC2 and PC3. The data are colored by either trial time (left) or session time (middle) to further validate that these different timescales are represented by orthogonal axes. Schematic (right) shows how activity can repeat across trials while simultaneously drifting in an orthogonal direction. (I) In the odor sequence task, rats were trained to run self-paced laps starting with a 10-s treadmill period, then retrieving a buried chocolate reward in an odorized cup of sand, and finally returning to the base of the maze for a small milk reward. Each lap constituted one trial. Five odors were presented on consecutive laps forming a sequence that was followed by a 5-min rest off of the maze. Each session contained three sequence runs, yielding a total of 15 laps. Schematic (right) shows hierarchy of timescales from a few seconds to many minutes. (J) Example session showing that sequence runs traced parallel neural trajectories through state space in the LEC, which could serve to link temporal contexts. Dots represent average activity for each trial. Points are colored from light to dark to show time within the session. Trial type and session time were approximately orthogonal. (K) Matrices showing distance traveled (ambient space) in the LEC between each of the 15 trials in an example session (left) and averaged over all sessions (right; $n = 10$ sessions). Note that drift continues throughout the session. Hatching as in Fig. 1C. (L) Distance traveled (ambient space) in the LEC as a function of lag in number of trials for all sessions. Main effect of lag: $F(13, 117) = 17.18$; $P = 1.89 \times 10^{-21}$, repeated measures ANOVA; $n = 10$ sessions. Arrows indicate local deviations (>1 SD) in residuals of a polynomial fit when the same trial type (odor) repeats and LEC activity states become closer together. [(C), (D), (G), and (L)] Data are represented as means \pm SEMs. *** $P < 0.001$, ** $P < 0.01$; ns, not significant.

the two vectors was $\sim 90^\circ$ (orthogonal), significantly larger than the variability calculated within each coding dimension using a resampling procedure ($\sim 15^\circ$; Fig. 4G and Materials and methods). In a complementary approach, we applied PCA to the trial-based data (1-s bins) and asked whether any of the top principal components were well correlated to either trial time or session time. In some cases, there were strong correlations to both trial time and session time, such that we could visualize both coding dimensions in a single two-dimensional (2D) subspace defined by those principal components (Fig. 4H and fig. S11F), which are orthogonal by definition. Combining these two orthogonal coding dimensions yields a helical trajectory, where each coil of the helix represents the recurring activity for one trial, and the long axis of the helix represents continuous drift throughout the session (Fig. 4H and fig. S11, F and L).

Real-world experiences, however, do not contain a single recurring event (e.g., one reward per trial), but rather consist of many different events across diverse timescales. To test whether LEC activity could evolve simultaneously along a larger number of trajectories, we used the odor sequence task described above, in which recurring hierarchically organized events spanned timescales of seconds to many minutes (Fig. 4I). Animals first ran in place on a treadmill for 10 s. Next, they ran one lap around the figure-eight maze, stopping to sample an odorized cup of sand and dig for a buried chocolate reward. The odor changed on each lap such that the odors formed a sequence over five laps from odor A to odor E. Finally, they performed three sequence runs (i.e., 15 total trials) with a 5-min rest between runs.

At the short timescale of seconds, LEC activity exhibited repeating trajectories during each trial. LEC activity was more similar across trials for matched trial times (i.e., the same 1-s time bin across different trials) compared with mismatched trial times (fig. S12A). These trial-based trajectories were similar to those in the figure-eight task above but extended for ~ 30 s (see example in Fig. 3D), which demonstrates that LEC activity can capture the fine temporal details of extended experience. Trajectories were also aligned (ambient space) across repeated periods on the treadmill in the absence of overt changes in the external environment (fig. S12B). Time on the treadmill could be accurately decoded (ambient space) from held-out trials using a k -nearest neighbors classifier (fig. S12C).

At the long timescale of minutes, LEC activity drifted, as in all tasks described above (fig. S12D). The activity evolved smoothly from one trial to the next along a linear trajectory during the first sequence run. After a 5-min rest, however, the activity reset near the starting point of the original trajectory and evolved along an approximately parallel trajectory during the second (and third) sequence run(s) (Fig. 4J). To quantify this relationship, we calculated the pairwise distance (ambient space) between all trials (Fig. 4K). The continuous drift caused larger distances between trials at increasing lags, with the exception that distances became closer together when the same trial type repeated (Fig. 4L), consistent with the notion of parallel (aligned) sequence trajectories. These sequences were much less apparent in the MEC and CA1 (fig. S12, E to G). Although odors likely contribute

to distinct LEC activity for each trial type (30), the increase in distance with increasing lag suggests that odor responses alone are insufficient to create the temporally ordered sequential representation described here.

Slow single-cell dynamics underlying drift

We next set out to identify mechanisms that might underly drift in LEC population activity. We previously found that a subset of LEC neurons exhibited monotonic changes in firing rate over the course of minutes (13). Although the variable time constants of these "ramping" neurons could conceivably drive population drift (31), in this study, we took a more general approach to quantify any pattern of firing rate variability over a timescale of minutes, matching the observed population drift. To do so, we calculated the fano factor (i.e., variance over mean) of the smoothed firing rate (Gaussian width = 30 s) for each neuron. Activity traces for LEC neurons with high variability took a variety of forms, including ramping, multi-peaked activity, and transitions between sustained periods of (in)activity (Fig. 5A and figs. S13 and S14). LEC neurons had significantly higher variability than MEC neurons (Fig. 5B), whereas CA1 neurons were intermediate, mirroring the differences in population drift shown above. Minute-scale dynamics were not restricted to a defined subset of LEC neurons but rather were broadly distributed throughout the population (figs. S13 and S14). Moreover, different neurons were maximally active at different times during the session (fig. S14C). By subsampling neurons on the basis of their variability, we found that these slow dynamics in single neurons are both necessary and sufficient for population drift (Fig. 5, C and D; fig. S14D; and fig. S15). The slow single-cell dynamics themselves may be a result of asymmetric connectivity within the network, behavioral timescale synaptic plasticity (32), or slowly changing inputs.

Synchronous ensemble responses underlying shifts

We next searched for a mechanism underlying shifts at event boundaries (13, 21) by examining the fraction of the population that responds at the boundary, the form of the responses, and whether the same neurons are active in the same pattern at each boundary. We characterized the responses of individual neurons on a trial-by-trial basis for each trial-based task. In the figure-eight task, 27% of neurons exhibited large increases or decreases in firing rate coincident with the shift in population activity as the rat approached the reward (Fig. 6A and fig. S16A). In terms of both the fraction of responding neurons and the magnitude of the rate changes, single-neuron responses were largest at the time of the shift compared with all other time points (Fig. 6A, right). Similar results were obtained in the odor sequence task and the novel objects task, where ensembles of positively or negatively modulated neurons responded at the time of the population shift (i.e., reward approach or object contact) (Fig. 6, B and C, and fig. S16B). To determine whether distinct activity patterns are expressed at successive event boundaries (33), we calculated the trial-to-trial variability in firing rate for boundary-modulated neurons. We restricted our analysis to the figure-eight task, where each event boundary within a

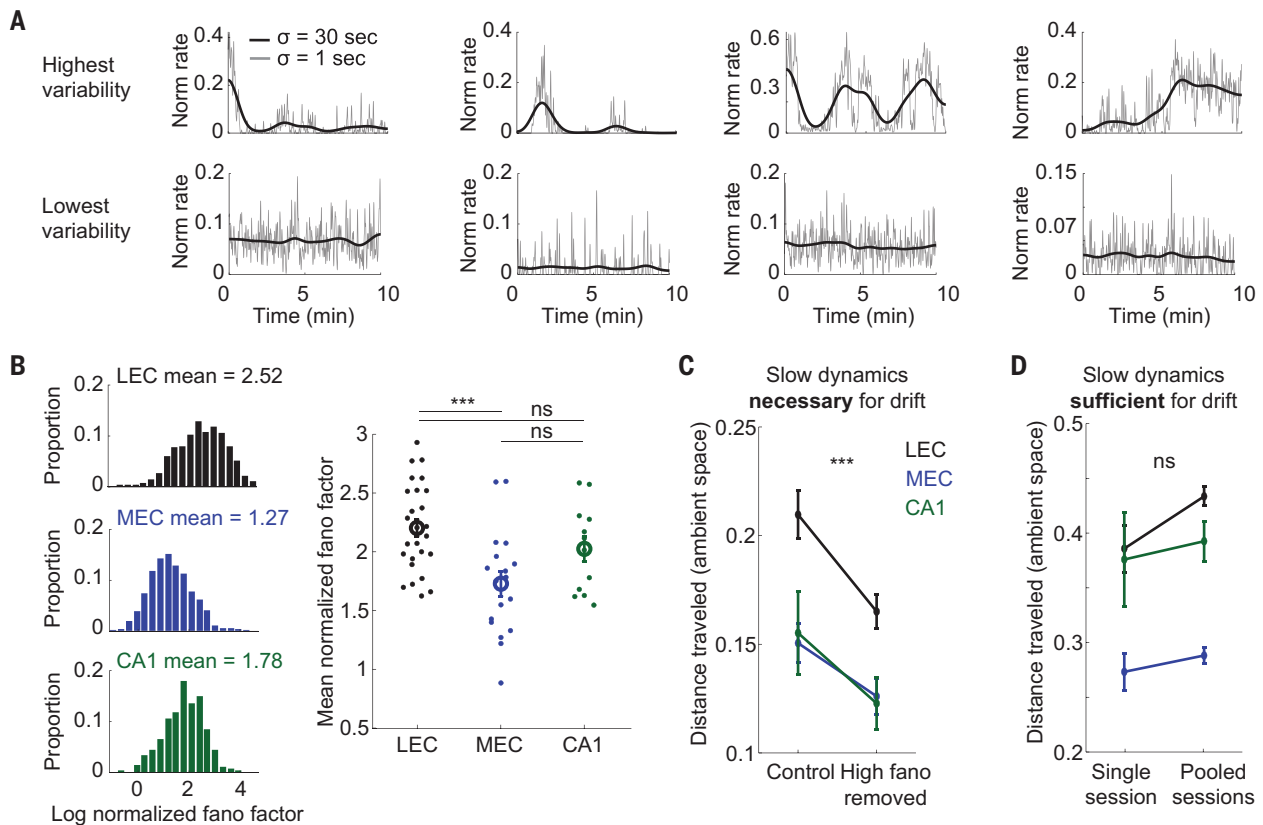


Fig. 5. Slow dynamics in individual neurons underlying population drift. (A) Activity traces for the four LEC neurons with highest (top) and lowest (bottom) levels of firing rate variability over a scale of minutes in the foraging task. Firing rates smoothed with 30-s (black) or 1-s (gray) Gaussian. (B) Minute-scale variability for each neuron in an example foraging session (left) and mean variability across neurons within each session (right) for each brain area. Variability over minutes quantified as log fano factor normalized to a homogeneous Poisson neuron such that 0 is same as Poisson. LEC versus MEC: $t(42) = 3.79$; $P = 4.80 \times 10^{-4}$. LEC versus CA1: $t(36) = 1.36$; $P = 0.18$. MEC versus CA1: $t(28) = -1.89$; $P = 0.07$. Two-sample *t* test; $n = 26, 18,$ and 12 sessions for LEC, MEC, and CA1, respectively. (C) Distance traveled (ambient space) was recalculated after subsampling from all cells within a session (control) or from a population that had the top 25% most variable cells removed (high fano removed). Removing the most variable neurons led to a significant decrease in distance traveled, indicating that slow dynamics in single cells are required for population drift. Main effect between control and high fano removed: $F(1, 53) = 80.16$; $P = 0$ (no bootstraps exceeded observed statistic), bootstrap repeated measures ANOVA; $n = 26, 18,$ and 12 sessions for LEC, MEC, and CA1, respectively. (D) Distance traveled (ambient space) was recalculated after subsampling the top 25% most variable cells within a session (single session) or from those same neurons pooled across all sessions (pooled sessions). This pooling effectively destroys the true correlation structure of the network and averages away sensory inputs that are specific to each experience, yet the amount of drift was not reduced. Slow dynamics are therefore sufficient for drift, whereas distinct experiences and specific cell-to-cell correlation structures are not required. Main effect between single and pooled: $F(1, 108) = 3.77$; $P = 0.19$. Bootstrap two-way ANOVA; $n = 26, 18,$ and 12 sessions for LEC, MEC, and CA1, respectively. [(B) to (D)] Data are represented as means \pm SEMs. *** $P < 0.001$; ns, not significant.

session is identical (i.e., same reward every lap). Boundary-modulated responses exhibited considerable variability across trials such that different cells responded at different event boundaries (Fig. 6, D and E, and fig. S16). These responses were significantly more variable across trials compared with responses in subsets of neurons that preferred times other than the shift (Fig. 6E). This suggests that although boundary-modulated neurons have similar activity on average across similar events (Fig. 6, A to C, and fig. S16, A and B), they also display enough trial-to-trial variability to assign a distinct time stamp to each individual event (Fig. 6D and fig. S16). In agreement with this notion of time-stamping, we could successfully decode individual events (trials) using a *k*-nearest neighbors classifier on held-out time bins (ambient space; Fig. 6F and fig. S16, C, D, and F).

Discussion

Leveraging the power of high-density, multiarea unit recordings in freely behaving rats, we have shown how neural population dynamics in the LEC depend on both intrinsic factors and the structure of the animal's experience. When experimental conditions were stable, neural

population activity in the LEC drifted progressively along a nonperiodic 1D manifold, regardless of the animal's current task or behavioral state. The fact that drift persisted during sleep, when external sensory inputs are minimal, points to an intrinsic origin of the changing population activity. In the awake state, the continuity of the drift was frequently interrupted by event boundaries—major transitions in the animal's experience, such as encountering a reward or a novel object. These nonlinearities in the neural trajectory segment the stream of experience into discrete events, which can be stored and later recalled as individual units in time (7, 10, 24).

The combination of drifting and shifting dynamics was expressed most strongly in the LEC, though the regional differences were, in most cases, only quantitative. Neural trajectories in the LEC may shape activity in the CA1 and MEC—regions that are known to exhibit temporal coding under certain conditions (8–12, 34, 35). The data are consistent with studies of the human hippocampus, in which sharp onset and offset responses at event boundaries (10, 16, 21–23) have been identified as a potential source of bias in future judgments of temporal order (21). The present large-scale recordings from animals

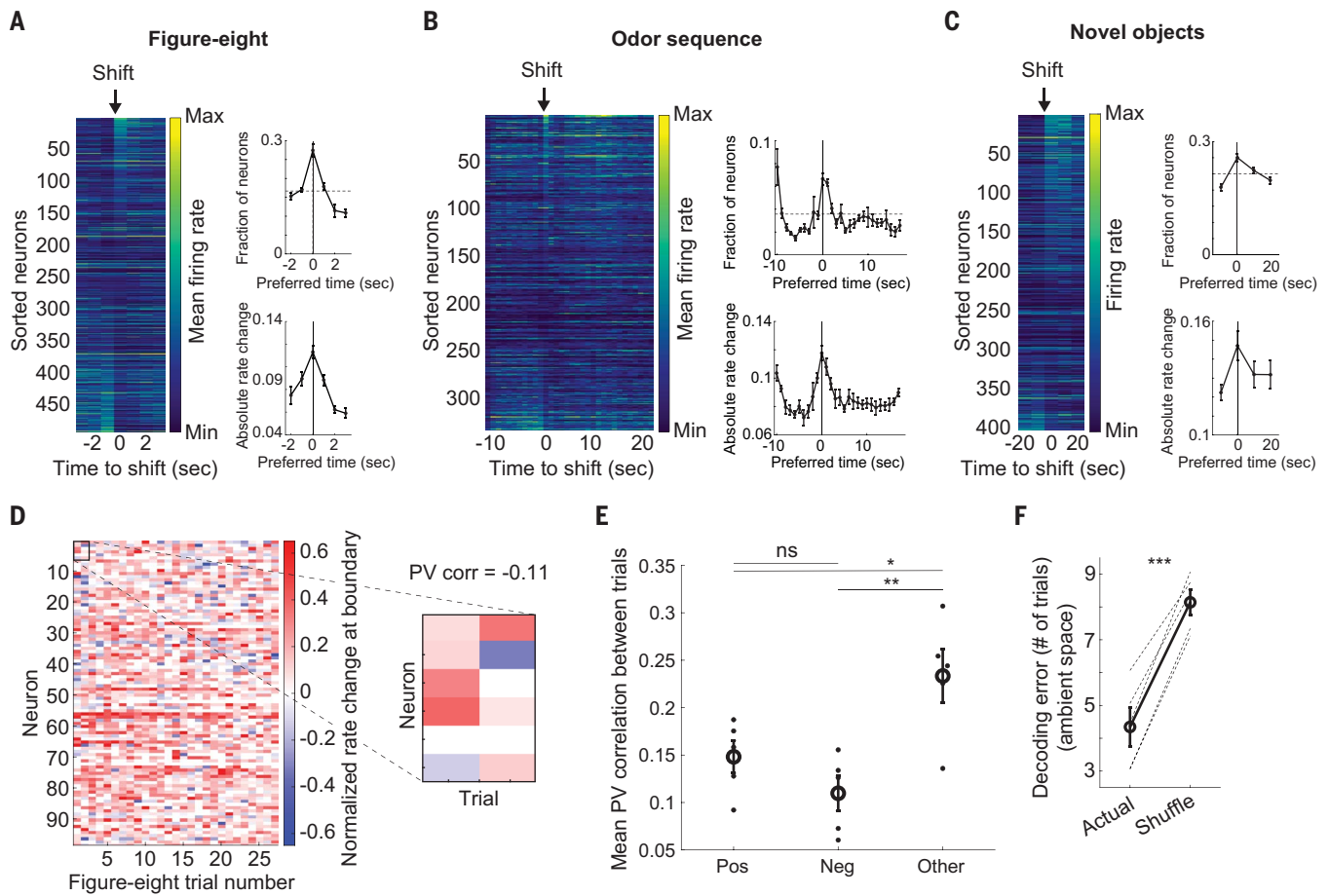


Fig. 6. Fast dynamics in individual neurons underlying shifts at event boundaries. (A) Example heatmap (left) of trial-averaged firing rate for all LEC neurons relative to reward in the figure-eight task. Sorting neurons by rate change at the time of population shift (relative to the preceding time bin) reveals both positively and negatively modulated neurons. Across all sessions, more neurons had their largest rate change at the time of the shift compared with all other trial times (top right). Horizontal line indicates the chance level of preferring each time bin. The absolute rate change was also highest for neurons that changed most at the time of the shift compared with all other times (bottom right). (B) Example heatmap (left) and summary data (right) showing LEC neurons modulated at the reward-related population shift in the odor sequence task. The initial peak on the left corresponds to the other population shift when the treadmill turns on. Conventions are as in (A). (C) Example heatmap (left) and summary data (right) showing LEC neurons modulated at the contact-related shift in the novel objects task. Conventions are as in (A). [(A) to (C)] Modulated neurons are defined as those with their largest absolute change in rate (relative to previous time bin) at the shift time (vertical lines). Chance level fractions (horizontal lines) were 17%, 4%, and 17% for figure-eight, odor sequence, and novel objects tasks, respectively, based on the number of time bins in each task. (D) Example data from figure-eight session showing that even after selecting for LEC neurons with trial-averaged increases in firing rate at the event boundary, this subset showed substantial trial-to-trial variability. Note the blue areas showing individual trials when these positively modulated neurons actually showed negative responses. The inset to the right highlights six example neurons for the first two trials with a population vector (PV) correlation of -0.11 , demonstrating that LEC activity creates distinct time stamps for each trial. (E) Mean PV correlation between LEC responses at event boundaries during figure-eight trials for positively modulated neurons (pos), negatively modulated neurons (neg), and randomly chosen subsets ($n = 25$) of neurons that preferred times other than the shift (other). Pos versus neg: $t(8) = 1.53$; $P = 0.17$. Pos versus other: $t(8) = -2.60$; $P = 0.03$. Neg versus other: $t(8) = -3.70$; $P = 6.01 \times 10^{-3}$, two-sample t test; $n = 5$ sessions. (F) Distinct time stamps for each event enabled accurate decoding (ambient space) of trial number in the LEC using a k -nearest neighbors classifier trained on held-out data (trials). Decoding error is measured as the difference between actual and predicted trial number. Shuffle obtained by shuffling epoch labels. Actual versus shuffle: $t(4) = -10.698$; $P = 3.90 \times 10^{-4}$, paired t test; $n = 5$ sessions. [(A) to (C), (E), and (F)] Data are represented as means \pm SEMs. *** $P < 0.001$; ** $P < 0.01$; * $P < 0.05$; ns, not significant.

identify discontinuities in the progressive drift of neural activity in the LEC and hippocampus as a candidate mechanism for the segmentation of experience into discrete episodic memories, as reported in human participants.

Our findings yield insight into the geometry of drift in neural state space. LEC population activity did not simply drift uniformly across the session. During tasks with repetitive temporal structure, activity also traveled (at a faster timescale) in directions orthogonal to the drift, enabling the system to encode temporal information about the task together with the slower changes reflecting session time. By traveling in independent directions for each behaviorally relevant

timescale, the neural code in the LEC is thus inherently multiscale, with fast timescales nested inside slow timescales. Multiscale temporal coding has been studied extensively in other regions at the level of neural oscillations (36–38), but few studies have explored longer timescales of seconds to minutes. Our findings show that activity can progress along multiple timescales also under nonperiodic conditions. Individual LEC neurons were not obviously locked to a single preferred timescale but instead flexibly expressed multiple timescales of experience, potentially allowing any target neurons to continuously capture the temporal statistics of the task. This hierarchical coding scheme could facilitate our ability to deconstruct events into subevents (17) at

timescales ranging from seconds to minutes or more and may be used to organize event information while it is stored in memory.

Finally, we identified candidate mechanisms underlying both continuous drift and abrupt shifts in LEC neural trajectories. Drift was associated with slow, minute-scale variability in the firing rates of individual neurons. Although a subset of these neurons displayed gradual ramping with different time constants (13, 31), most neurons had a variety of other forms of slow dynamics. The richness of these dynamics may reflect properties of the individual neurons or synaptic changes in the network (32). In contrast to the slow drift, the abrupt shifts in neural trajectories were associated with synchronous responses of groups of neurons at event boundaries. These synchronous responses may be elicited by external inputs targeting subsets of LEC neurons, reflecting the LEC's position as a node of convergence for afferents from widespread cortical and subcortical regions (39, 40). They might also be induced by neuromodulatory arousal systems in the brainstem associated with novelty and prediction error (41–44). Regardless of whether the inputs are sensory or neuromodulatory, however, the combination of activated LEC cells was distinct at each event boundary, which suggests that the discretization of neural trajectories in the LEC does not merely reflect nonspecific arousal. When read out by neural circuits downstream in the hippocampus, experiences between the individually tagged boundaries may therefore be stored and retained as individual, orthogonalized episodic memories (33, 35, 45, 46). These units of memory may then form the basis for reconstructive estimates of duration and temporal order during recall of experience (7).

Materials and methods

Subjects

The data were collected from nine adult (~12- to 18-week-old) male Long Evans rats weighing ~400 to 500 g at time of implantation. The rats were group-housed with one to eight of their male littermates before surgery and were housed alone in a large two-story enriched metal cage (95 × 63 × 61 cm) thereafter. Rats were handled daily. They were kept on a 12-hours light–12-hours dark schedule, with strict control of humidity and temperature. All experiments were approved by the Norwegian Food Safety Authority (FOTS ID 18011) and performed in accordance with the Norwegian Animal Welfare Act and the European Convention for the Protection of Vertebrate Animals used for Experimental and Other Scientific Purposes.

Surgery and electrode implantation

Rats were implanted with Neuropixels 2.0 silicon probes targeting the LEC, MEC, and/or CA1. One rat (27284) had a Neuropixels 1.0 single-shank probe implanted in the MEC. LEC probes were implanted 6.23 to 7.00 mm posterior to bregma, 3.70 to 4.05 mm lateral of the midline, at an angle of 20° in the coronal plane with the tip of the probe pointing laterally. Probes were lowered until one or more shanks met resistance at the ventral surface and were then retracted 100 μm, reaching a final depth 7.84 to 9.11 mm below the pial surface. MEC probes were implanted 100 μm anterior to the transverse sinus, 4.60 mm lateral of the midline, at an angle of 26° in the sagittal plane with the tip of the probe pointing anteriorly. Probes were lowered 5.50 mm below the pial surface. CA1 probes were implanted 3.80 mm posterior to bregma and 3.20 mm lateral of the midline. Probes were lowered 6.00 to 6.19 mm below the pial surface. Table S1 reports the exact implant coordinates for each probe in each rat. The implant was secured with dental cement. A small stainless-steel screw was attached to the skull above the cerebellum and connected to the probe ground and external reference pads with insulated silver wire. See (25) for further details of probe implantation. After surgery, rats were left to recover until resuming normal locomotor behavior, a minimum of 2 hours. Postoperative analgesics (meloxicam and buprenorphine) were administered during recovery.

Recording procedures

The details of the Neuropixels hardware system and the procedures for freely moving recordings have been described previously (25, 47). In brief, electrophysiological signals were amplified with a gain of 80, filtered 0.005 to 10 kHz, and digitized at 30 kHz by the probe's on-board circuitry. The digitized signals were multiplexed by an implant-mounted headstage circuit board and were transmitted along a lightweight 5-m tether cable, made using twisted pair wiring. SpikeGLX software (<https://billkarsh.github.io/SpikeGLX/>) was used for data acquisition and configuring the probes. 3D motion capture (OptiTrack Flex 13 cameras and Motive recording software) was used to track the rat's head position and orientation by attaching a set of five retroreflective markers to the implant during recordings. The 3D marker positions were projected onto the horizontal plane to yield the rat's 2D position and head direction. An Arduino microcontroller was used to generate digital pulses, which were sent to the Neuropixels acquisition system [via direct transistor-transistor logic (TTL) input] and the OptiTrack system [via infrared light-emitting diodes (LEDs)] to permit precise temporal alignment of the recorded data streams. To analyze the animal's behavior in greater detail, an overhead Basler camera was also used for the natural sleep, odor sequence, and novel objects tasks described below. Movies were aligned to the neural and behavioral data post hoc using the same infrared LED pulses used for the OptiTrack system.

Behavioral procedures

Data were obtained from several recording sessions performed within the first week after recovery from surgery. Recordings were performed while the rats engaged in four behavioral paradigms (or sleep sessions) using multiple mazes/arenas and rooms. Many distal visual and auditory cues were available to the rat. During presurgical training and habituation, several of the rats were food-restricted through intermittent fasting during which food was available ad libitum for four hours between 12:00 and 17:30. During that training phase, behavioral procedures were done from 8:00 when the animals were maximally food motivated. Food restriction ceased a minimum of 24 hours before surgery.

Foraging task

Seven rats (26863, 26965, 26966, 27284, 27285, 27963, and 28003) foraged for randomly scattered food crumbs (corn puffs and vanilla cookies) in a square open-field arena with a diameter of 1, 1.5, or 2 m. The arena had dark blue or black wax/vinyl flooring and was enclosed by walls of height 50 cm. Large distal cues were available outside of the arena near the room walls. The arena was dimly lit by one or two lamps along the room wall. At the time of surgery, four rats (27284, 27285, 27963, and 28003) were familiar with the environment and task (minimum four × 10 min sessions). Three rats (26863, 26965, and 26966) were completely naïve to the arena, room, and task at the time of their first recording session (these three recordings are not analyzed). Recording sessions lasted between 12 and 142 min.

Natural sleep

Six rats (27284, 27285, 27963, 28003, 29629, and 29630) were recorded during natural sleep by placing them in a dedicated sleep box made of black acrylic (30 × 30-cm floor, 80 cm height). The floor contained a shallow flowerpot lined with several towels to make a nest and rats were habituated to the box over a minimum of four sessions before implantation. The box walls passed infrared light to enable tracking through the walls. Room lights were on and pink noise was played through the computer speakers at ~60 dB to mask background sounds. Sleep sessions were conducted at the end of the light phase (7:00 to 8:00) and lasted between 45 and 180 min.

Figure-eight task

Two rats (26965 and 26966) were trained to run laps around a figure-eight maze, receiving one reward per lap. The maze was made of wood

with vinyl flooring and plastic lips (2 cm high) and was elevated 80 cm above the ground by metal table legs. After being placed at the base of the maze, rats ran down a 50 cm long (12 cm wide) central stem to the top of the maze which was a 50 × 50 cm square with a small reward port (polyurethane tubing leading to 15 ml conical tube cap) at the far end. After drinking a sweetened chocolate milk reward (2.5% sucrose in Oatly chocolate milk), the rat could run back along either return arm (12 cm wide) to reach the base of the central stem again. The maze was open to the room with many available distal cues. The room was dimly lit by two small lamps on the left room wall. Animals were prevented from running in the wrong direction using a tall plastic barrier during training. During training and testing, a large plastic door was also used at the top of the central stem to prevent backtracking. The door opened as the rat came down a return arm and closed again after the rat retrieved a reward. Animals were considered trained when performing ~20 trials per session for multiple days and were implanted shortly thereafter.

Odor sequence task

Two rats (27285 and 29630) were trained to run laps around the same figure-eight maze described above, with a few small modifications. A milk port was added at the base of the central stem. The central stem itself was a treadmill with a large front door to prevent the rat from leaving until the treadmill turned off. At the top of the maze, the rat was presented with an odorized cup of sand containing a buried chocolate cookie crumb reward (ChocoLoops). Odors were 1 of 10 common household spices, thoroughly mixed in sand with the following concentrations: A = parsley, 1%; B = cumin, 0.5%; C = paprika, 1%; D = thyme, 1%; E = cardamom, 0.8%; L = clove, 0.5%; M = tarragon, 1%; N = cinnamon, 0.8%; Ø = dill, 1%; P = coffee, 1%. For rat 29630, two changes were made: odor C was cinnamon (0.8%) and odor N was basil (1%). A custom GUI written in MATLAB was used to control the treadmill, door, and milk delivery. Each trial began when the rat reached the end of the treadmill, which triggered the treadmill to turn on at 30 cm/s for 10 s. After 10 s, the treadmill turned off, and the large front door opened so the rat could run to the sand cup to dig for a reward. The rat then ran via either return arm to receive a sweetened chocolate milk reward (2.5% sucrose in Oatly chocolate milk) at the base of the central stem, before entering the treadmill again to initiate another trial. On each trial the odor in the sand was different, creating a sequence of five odors A through E across five trials. Sand and odors from the previous trial were removed with a handheld vacuum during the 10 s treadmill run, after which the sand cup for the next trial was put in position. This ensured that the rat could not smell the upcoming odor or chocolate treat until after leaving the treadmill. These five trials comprised a run, and the rat ran three runs with 5 min rest in a towel-covered flowerpot between each run, and also before and after the runs: rest, RUN1, rest, RUN2, rest, RUN3, rest. The rat ran this sequence (SEQ1) in the morning, and after a 2-hours delay in the home cage, returned to run a second sequence (SEQ2) in the afternoon. The only difference between morning and afternoon is that SEQ2 contained five different odors L through P. Data from the two different sequences were treated equivalently for analysis purposes. Shaping to dig and run laps took several days. Training on the full task with both sequences occurred over several days and surgery was conducted after training day 3. Recordings lasted ~30 min for each sequence.

Novel objects task

Four rats (27963, 28003, 29629, and 29630) foraged for randomly scattered food crumbs (corn puffs and vanilla cookies) in a square open-field arena, exactly as in the foraging task described above. After 7.5 min of foraging in the empty arena, a novel object was placed at a pseudorandom location on the floor of the arena. Objects had footprints of ~10 × 10 cm and were ~15 cm tall. They consisted of common laboratory or household items (e.g., beaker, flask, spray bottle, candlestick).

7.5 min later that object was removed and another novel object was placed at different pseudorandom location. This was repeated once more 7.5 min later resulting in the following sequence: Empty, OBJ1, OBJ2, OBJ3. Recordings therefore lasted 30 min. At the time of surgery, the rats had never experienced objects in the arena before. Two rats (27963 and 28003) were familiar with the foraging task (minimum four × 10 min sessions) from presurgical habituation, whereas the others had no prior experience in the foraging task. The experiment was repeated for each rat to maximize the number of novel object contacts (number of sessions and contacts reported in table S2).

Spike sorting and unit selection

Spike sorting was performed with KiloSort 2.5 with customizations as previously described (47). Units were discarded if >2% of their interspike interval distribution consisted of intervals <2 ms. In addition, units were excluded if they had a mean spike rate of <0.05 Hz or >40 Hz (calculated across the full recording duration), or if they were recorded on sites outside the region of interest. LEC recordings included units from both superficial and deep cell layers (figs. S1 to S3). No attempt was made to segregate principal cells from interneurons.

Preprocessing and temporal binning

Data were not filtered for running speed. Spikes were binned using 0.01- to 10-s time bins, depending on the timescale of interest for each task, and tracking data were resampled at the same time intervals to align them with the spike data. Bin size is indicated in the figures and their legends. Spike count vectors for each neuron were “soft” normalized (48) to reduce the impact of strong responses by dividing the counts by the range of counts +5, where 5 is the normalization factor. Analyses therefore capture variance in neural responses more than their absolute firing rates. Spike time matrices for each region consisted of all units that met the selection criteria above.

Neural populations were not pooled across recording sessions. By restricting the analysis to populations of simultaneously recorded neurons, we avoided potential spurious results caused by mixing recording sessions of neural activity in different functional modes. The one exception to this rule is the analysis presented in Fig. 5D which shows that pooling neurons across recording sessions does not eliminate drift at the (pseudo)population level.

Sleep stage classification

Sleep stages were identified as described previously (47). Periods of sustained immobility (lasting >120 s; locomotion speed, <1 cm/s; head angular speed, <0.1 rad/s) were classified into SWS and REM based on the theta (5 to 10 Hz)/delta (1 to 4 Hz) ratio of MEC or CA1 population activity (theta is notably absent in the LEC). Periods when the theta/delta ratio remained above 1.0 for at least 20 s were classified as REM, whereas periods when the theta/delta ratio remained below 0.8 for at least 20 s were classified as SWS (see fig. S7A for sleep stage classifications in all animals).

UP or DOWN state classification during SWS

To classify SWS activity between active UP states and quiescent DOWN states, the spiking activity of each LEC neuron during sleep was first binned at 25-ms resolution. LEC population firing rate was calculated in each bin for each segment of SWS (defined above in Sleep Stage Classification). A threshold was set at the 10th percentile of the population firing rate distribution. Periods lasting at least 125 ms with population rate above the threshold were classified as UP states, whereas those below the threshold were classified as DOWN states.

Matched data to compare drift between states

REM segments showed extensive variability in total duration, with several of them lasting either <10 s or >60 s (fig. S7E). To robustly quantify

drift and evaluate its similarity to wake states, REM segments lasting a minimum of 72 s were sampled from all animals. We then randomly sampled 60 s from these longer REM periods, excluding the first and last 6 s to avoid potential contamination from other states due to imperfect sleep stage classification. These segments of exactly 60 s were binned at 1-s resolution. For each REM segment included in the dataset, an equally long segment was randomly sampled from a foraging session of the same animal and binned at 1-s resolution. As done for the REM data, the beginning and end of the foraging session (first 2 min or last 1 min) were excluded to avoid variability due to the event boundary effects shown in Fig. 3B.

For each matched REM and foraging segment, several measures were quantified to compare drift. Distance traveled (Fig. 2, E and F; fig. S7G; and fig. S8, A, B, F, and G), decoding of temporal epochs (Fig. 2G and fig. S8C), and tangling of neural trajectories (fig. S7H and fig. S8H) were calculated following the exact same procedures described above. The only difference was the temporal bin sizes decreasing by a factor of 10 due to the short durations (1-s bins, 6-s epochs, 60-s segment duration). Additionally, the same 60-s REM and foraging segments were binned at 2-s, 500-ms, and 100-ms resolution to show that the similarity in distance traveled between states was insensitive to these choices of bin size (fig. S7F and fig. S8E).

Definition of trial data from continuous behavior

Trials in the figure-eight task were defined post hoc from continuous lap running behavior. Trials were aligned based on the x - y position of the rats (from head-mounted markers) just before stopping to consume the reward. This point was calculated by finding the mode of the distribution of all y -position values throughout the session when the rat was within a defined x -position range capturing the central stem. It was confirmed by manual inspection that this corresponded to the location of reward consumption. The trial alignment point was then defined as 3 cm below that location to ensure exclusion of reward consumption itself in some analyses. For analysis of shifts in state space (Fig. 3 and figs. S9 and S10), trials were defined from 3 s before the alignment point to 4 s after (including reward). For analysis of within-trial time (Fig. 4 and fig. S11), trials were defined as the 6-s periods leading up to the alignment point (excluding reward).

Trials in the odor sequence task were defined based on logged time stamps of the treadmill turning on. Each trial started when the treadmill turned on and ended either when the treadmill turned on for the next trial, or when it was the final lap of the sequence run, after consuming the reward at the top of the maze (thus the final laps were shorter than the rest). For comparing activity across trials, trials were truncated to the fastest full lap. For observing the full dynamics in Fig. 4J and fig. S12E, all times during sequence runs and intertrial intervals were included.

There were not trials in the novel objects task, yet neural and behavioral data were aligned to moments of object contact/exploration. Contact was defined as the tracked position of the head being within a 10-cm radius of the center of an object. Note that because objects had footprints of $\sim 10 \times 10$ cm, and the tracked position of the head was centered on their skull, the 10-cm radius effectively ensured the animal was in contact with the object [e.g., (10-cm radius) – (5 cm of object) – (3 cm from head to nose) = ~ 2 cm distance]. These contacts were further validated in video recordings and involved whisking, nose poking, rearing onto the object, and occasionally climbing onto the object.

Distance traveled and change in trajectory speed

Distance traveled was defined as the cosine distance (using the SciPy or MATLAB function *pdist*) between population vectors in the ambient space (dimensionality equal to the number of simultaneously recorded neurons). Values range between 0 (identical vectors) and 1 (orthogonal

vectors). Cosine distance is a common metric used in high-dimensional data where data are most often concentrated near the perimeter instead of the origin. Preliminary data exploration using other metrics yielded qualitatively similar results. For comparisons between temporal epochs consisting of multiple time bins, distance was calculated as the mean pairwise distance between the epochs.

Change in trajectory speed (acceleration or deceleration) was defined as the second derivative of distances between population vectors for neighboring time bins. Agnostic search for event boundaries was done by calculating the instantaneous change in trajectory speed throughout the whole recording session. Putative times for discrete shifts in state space were defined as those when the population firing rate exceeded the 90th percentile and the increase in population firing rate from the previous time bin also exceeded the 90th percentile (different choices of threshold yielded similar results). The increase compared with the previous time bin was important for capturing changes in activity as opposed to continuous periods of elevated activity. The reason for focusing further on times when population firing rate was high was to avoid times when the network was simply recovering to baseline after brief moments of reduced activity, which were regularly observed in LEC activity. Change in trajectory speed at those onsets of synchronous activity were compared with all other times in the recording session.

Neural trajectory alignment

Neural trajectory alignment was used to assess whether matched trial data were closer together in state space compared with mismatched trial data.

Matched distances were defined as the mean pairwise cosine distance (ambient space) between time bins with matched temporal epochs across different trials (e.g., the first 1-s time bin of each trial in the figure-eight task). Mismatched distances were calculated in the same manner but for time bins with mismatched temporal epochs across different trials (e.g., the first 1-s time bin of trial 1 compared with the fourth 1-s bin of trial 2). The magnitude of the difference between these values was rather small because mismatched distances included comparisons of neighboring temporal epochs where distances are expected to be small.

Decoding of temporal epochs

Decoding of temporal epochs was done in the ambient space of recorded neurons. Data were split into five cross-validation folds using the sci-kit learn function *KFold*. For decoding time within a session or trial number, time bins were shuffled before splitting into folds so that training data consisted of time bins from several temporal epochs. For decoding time within a trial or trial type, data were split into five folds based on trials such that entire trials were held out of the training data. The decoder used was *KNeighborsClassifier* from sci-kit learn with the following parameters: $n_neighbors = 10$, $weights = "distance"$, $metric = "cosine"$. Temporal epochs were predicted for each time bin using the sci-kit learn function *cross_val_predict*. Decoding accuracy was defined as the percentage of correctly predicted epochs, averaged over the five folds, using the sci-kit learn function *accuracy_score*. Decoding error was defined as the mean difference in time between predicted and actual epochs.

Dimensionality reduction

Dimensionality reduction was used only for visualizing neural trajectories, quantifying tangling of trajectories, and calculating the offset between coding dimensions. Distances between neural states (see above) were always calculated in the ambient space to avoid potential distortions in lower dimensional embeddings.

PCA was run on the soft normalized spike \times time matrices for each region using the sci-kit learn function *PCA*. LDA was used to find dimensions capturing change over time using the sci-kit learn function

LinearDiscriminantAnalysis. Principal components explaining 50% of the variance were used as input to LDA and class labels were defined as temporal epochs (foraging = 1 min, sleep = 6 s, figure-eight = 1 s, odor sequence trial time = 1 s, odor sequence full dynamics = trial/intertrial number, novel objects = 1 min).

Note that these LDA projections only reveal differences between temporal epochs when neural activity is actually distinct during each temporal epoch. Shuffling the class labels provides one control for artifacts specific to the LDA projection.

Tangling of neural trajectories

Tangling of neural trajectories was calculated in the 2D space of the top two linear discriminants following PCA/LDA as described above. Tangling was defined as in (49)

$$Q(t) = \max_{t'} \frac{\|\dot{x}_t - \dot{x}_{t'}\|^2}{\|x_t - x_{t'}\|^2 + \epsilon}$$

where x_t is the population vector at time t , \dot{x}_t is the temporal derivative of the neural state, $\|\cdot\|$ is the Euclidean norm, and ϵ is a small constant that prevents division by zero. Note that values of Q are inversely proportional to the neural state distances. When comparing smaller temporal intervals, distances are expected to be smaller and therefore tangling values would be larger.

Angular offset between coding dimensions

The angular offset between coding dimensions (e.g., session or trial time; Fig. 4G) was defined by running PCA/LDA, as described above, for each coding dimension (CD) separately. The PC with the largest contribution to the top LD was identified and its PC loadings were extracted. The same procedure was done for the other CD. Angular offset was defined as

$$\text{Offset} = \cos^{-1}(|\text{Loadings}_{\text{CD1}} \cdot \text{Loadings}_{\text{CD2}}|)$$

The probability that any pair of vectors is orthogonal increases in higher dimensions. To avoid spurious claims of orthogonality, a leave-one-out resampling procedure was used to quantify the stability of each CD over time. For session time, loadings were recalculated after leaving out one temporal epoch. This was repeated for each temporal epoch. Within CD stability was defined as the median angular offset between each of the resampled vectors and the original vector. For trial time, loadings were recalculated after leaving out one trial. This was repeated for each trial. Within CD stability was again defined as the median angular offset between each of these resampled vectors and the original vector.

The angular offset approach was well-suited to identifying the best CD vector for each timescale, yet it required two separate sources of input data (full session data with 10-s bins versus trial-based data with 1-s bins). A complementary approach allowed us to observe the orthogonal CDs in a single common subspace (Fig. 4H and fig. S11F). PCA was run on the trial-based data with 1-s bins. Each of the top PCs were then examined to check for strong correlations with either trial time or session time. When such correlations were present, we could visualize both coding dimensions in a single 2D subspace defined by those PCs, which are orthogonal by definition.

Multiplexing of coding dimensions in individual neurons

Multiplexing of coding dimensions (e.g., session or trial time) was defined by running PCA/LDA, as described above, for each coding dimension (CD) separately. The PC with the largest contribution to the top LD was identified and its absolute PC loadings were extracted. The same procedure was done for the other CD. These loadings were plotted against each other for visualization and neurons exceeding the 75% percentile of both distributions of loadings were considered as potential multiplexing neurons (i.e., displaying mixed selectivity) (fig. S11M).

Neurons at the extreme ends of both distributions of loadings were further visualized as a proof of principle that multiplexing of these timescales is possible (fig. S11, N and O).

Minute-scale variability in neural firing rates

Individual neuron spike trains during 10-min foraging sessions were binned in 0.5-s bins and then smoothed with a Gaussian of width $\sigma = 30$ s. The fano factor of this smoothed firing rate vector was defined as

$$\text{fano} = \frac{\text{var}(\text{rate})}{\text{mean}(\text{rate})}$$

To compare these values with a known reference, synthetic spike trains were sampled from a homogeneous Poisson process and fano factors were calculated on these synthetic Poisson neurons in the same manner. Log normalized fano factor values reported in Fig. 5B were obtained by dividing the fano factor of each real neuron by the mean fano factor of 500 synthetic Poisson neurons, and then taking the log of this value. Based on this normalization, a value of 0 indicates the same amount of variability as observed in Poisson neurons.

Note that the fano factor is not a proxy of a neuron's time constant. For estimation of time constants, see below.

Estimation of time constants in individual neurons

Two methods were used to estimate time constants in individual neurons (fig. S14, A and B). For both methods, individual neuron spike trains during 10-min foraging sessions were binned in 0.5-s bins. The large bin size was used to focus on neural dynamics at the behavioral timescale of seconds to minutes.

The first method (fig. S14A) fit these unsmoothed, binned spike counts with a Poisson generalized linear model (MATLAB function *glmfit*). The model contained two predictors: (i) a linear function of elapsed time during the session and (ii) mean population firing rate over time of all simultaneously recorded neurons. Neurons significantly modulated ($P < 0.05$) by elapsed time were subsequently fit with a single-term exponential model, $f(x) = ae^{bx}$, where $f(x)$ is the firing rate, a and b are constant coefficients, and $1/b$ is the time constant. This method captures the overall time course of neural activity for neurons with simple exponential ramping profiles.

The second method (fig. S14B) calculated the autocorrelation of the unsmoothed, binned spike counts. The autocorrelation function was truncated to include only positive lags and then normalized by dividing by the maximum correlation value. A single-term exponential model with the same form as above was fit to the early decay portion of the autocorrelation function from 1 to 90 s (other ranges produced similar results), and the resulting time constant was extracted. This method captures the timescale of neural activity changes more generally and is agnostic to the overall time course.

Correlation structure

Pairwise correlations were calculated as the Pearson correlation between all pairs of smoothed firing rate vectors during individual 10-min foraging sessions (as defined in previous section). Pairwise correlations were also explored at finer temporal resolutions (1-s, 500-ms, and 100-ms bin sizes) and differences between brain areas were less pronounced. The notable differences between brain areas occurred at the behavioral timescale of minutes, which was the focus of this study.

Breaking correlation structure (fig. S15B) was done by circularly shifting unsmoothed firing rate vectors for simultaneously recorded neurons relative to each other. Each neuron was shifted in time independently by a random interval between -2 min and 2 min. The first and last 2 min of the spike \times time matrix was then truncated to eliminate edge effects from the shifting procedure, and distance traveled during the remaining 6 min of the foraging session was calculated as above.

Drift in synthetic networks

Synthetic spike trains ($n = 500$ units) were sampled from a homogeneous Poisson process, as described above. Each synthetic unit was then duplicated such that one copy was smoothed with a Gaussian of width $\sigma = 30$ s (slow) and the other copy was smoothed with a Gaussian of width $\sigma = 1$ s (fast). Example units are shown in fig. S15C. Neural trajectories and distance traveled over 10 min were calculated for slow and fast populations separately (fig. S15, D and E) using the same methods described above. This procedure was repeated for a total of 25 simulations, the results of which are individually displayed in fig. S15E.

Event boundary responses in individual neurons

The preferred time for each neuron in trial-based tasks was defined as the time bin with the largest absolute change in trial-averaged firing rate relative to the preceding time bin. The fraction of neurons preferring each time bin was calculated as the number of neurons preferring each bin divided by the total number of simultaneously recorded neurons (i.e., calculated per session). The absolute rate change was calculated as the mean absolute change in trial-averaged firing rate relative to the preceding time bin, calculated over all time bins, for all simultaneously recorded neurons. These measures all focus on trial-averaged responses and are presented in Fig. 6, A to C, and fig. S16, A and B.

Time-stamping of individual events was assessed by calculating the mean population vector correlation across all figure-eight trials for different subsets of simultaneously recorded neurons. Positively modulated neurons were defined as neurons with preferred times (defined in previous paragraph) at the event boundary that had a trial-averaged increase in firing rate at that time relative to the preceding time bin. Negatively modulated neurons were defined in the same manner for neurons with decreases in firing rate. Control populations were defined as random samples of 25 simultaneously recorded neurons, and mean population vector correlations were averaged over 50 random samples. Decoding of trial identity was performed as described above using all simultaneously recorded neurons. Decoding error was defined as the mean difference in trial number between predicted and actual epochs. These measures all focus on variability between trials and are presented in Fig. 6, D to F, and fig. S16, C to F.

Histology and recording locations

Rats were deeply anesthetized with isoflurane, given an overdose of sodium pentobarbital, and perfused intracardially with saline followed by 4% formaldehyde. The extracted brains were stored in formaldehyde and a cryostat was used to cut 30- μ m sagittal sections, which were then Nissl-stained with cresyl violet. The probe shank traces were identified in photomicrographs, and a map of the probe shank was aligned to the histology by using the tip of the probe shank as a reference point. The recorded area of the probe was near-parallel to the cutting plane; therefore, it was deemed sufficient to perform a flat 2D alignment in a single section. The aligned shank map was then used to calculate the anatomical locations of individual recording sites (figs. S1 to S3).

Data analysis and statistics

Data analyses were performed with custom-written scripts in Python 3.10 and MATLAB 2023a (MathWorks). Open-source Python packages used were: NumPy, SciPy, sci-kit learn, and pandas. Statistical analysis was performed in MATLAB or Python. Power analysis was not used to determine sample sizes. The study did not involve any experimental subject groups; therefore, random allocation and experimenter blinding did not apply and were not performed. Error is reported as standard error of the mean. Sample sizes are reported in the Results section. Assumptions of parametric tests (i.e., normality, homogeneity of variance) were formally tested. When these assumptions were

violated, alternative nonparametric tests or bootstrap resampling procedures were used instead.

REFERENCES AND NOTES

1. W. James, *The Principles of Psychology*, vol. 1 (Henry Holt and Co., 1890).
2. E. Tulving, W. Donaldson, *Organization of Memory* (Academic Press, 1972).
3. W. B. Scoville, B. Milner, Loss of recent memory after bilateral hippocampal lesions. *J. Neurol. Neurosurg. Psychiatry* **20**, 11–21 (1957). doi: [10.1136/jnnp.20.1.11](https://doi.org/10.1136/jnnp.20.1.11); pmid: [13406589](https://pubmed.ncbi.nlm.nih.gov/13406589/)
4. L. R. Squire, Memory and the hippocampus: A synthesis from findings with rats, monkeys, and humans. *Psychol. Rev.* **99**, 195–231 (1992). doi: [10.1037/0033-295X.99.2.195](https://doi.org/10.1037/0033-295X.99.2.195); pmid: [1594723](https://pubmed.ncbi.nlm.nih.gov/1594723/)
5. J. O'Keefe, L. Nadel, *The Hippocampus as a Cognitive Map* (Oxford Univ. Press, 1978).
6. E. I. Moser, M. B. Moser, B. L. McNaughton, Spatial representation in the hippocampal formation: A history. *Nat. Neurosci.* **20**, 1448–1464 (2017). doi: [10.1038/nrn.4653](https://doi.org/10.1038/nrn.4653); pmid: [29073644](https://pubmed.ncbi.nlm.nih.gov/29073644/)
7. A. Tsao, S. A. Yousefzadeh, W. H. Meck, M. B. Moser, E. I. Moser, The neural bases for timing of durations. *Nat. Rev. Neurosci.* **23**, 646–665 (2022). doi: [10.1038/s41583-022-00623-3](https://doi.org/10.1038/s41583-022-00623-3); pmid: [36097049](https://pubmed.ncbi.nlm.nih.gov/36097049/)
8. J. R. Manns, M. W. Howard, H. Eichenbaum, Gradual changes in hippocampal activity support remembering the order of events. *Neuron* **56**, 530–540 (2007). doi: [10.1016/j.neuron.2007.08.017](https://doi.org/10.1016/j.neuron.2007.08.017); pmid: [17988635](https://pubmed.ncbi.nlm.nih.gov/17988635/)
9. E. A. Mankin et al., Neuronal code for extended time in the hippocampus. *Proc. Natl. Acad. Sci. U.S.A.* **109**, 19462–19467 (2012). doi: [10.1073/pnas.1214107109](https://doi.org/10.1073/pnas.1214107109); pmid: [23132944](https://pubmed.ncbi.nlm.nih.gov/23132944/)
10. Y. Ezzayat, L. Davachi, Similarity breeds proximity: Pattern similarity within and across contexts is related to later mnemonic judgments of temporal proximity. *Neuron* **81**, 1179–1189 (2014). doi: [10.1016/j.neuron.2014.01.042](https://doi.org/10.1016/j.neuron.2014.01.042); pmid: [24607235](https://pubmed.ncbi.nlm.nih.gov/24607235/)
11. L. T. Hsieh, M. J. Gruber, L. J. Jenkins, C. Ranganath, Hippocampal activity patterns carry information about objects in temporal context. *Neuron* **81**, 1165–1178 (2014). doi: [10.1016/j.neuron.2014.01.015](https://doi.org/10.1016/j.neuron.2014.01.015); pmid: [24607234](https://pubmed.ncbi.nlm.nih.gov/24607234/)
12. W. Mau et al., The Same Hippocampal CA1 Population Simultaneously Codes Temporal Information over Multiple Timescales. *Curr. Biol.* **28**, 1499–1508.e4 (2018). doi: [10.1016/j.cub.2018.03.051](https://doi.org/10.1016/j.cub.2018.03.051); pmid: [29706516](https://pubmed.ncbi.nlm.nih.gov/29706516/)
13. A. Tsao et al., Integrating time from experience in the lateral entorhinal cortex. *Nature* **561**, 57–62 (2018). doi: [10.1038/s41586-018-0459-6](https://doi.org/10.1038/s41586-018-0459-6); pmid: [30158699](https://pubmed.ncbi.nlm.nih.gov/30158699/)
14. J. L. Bellmund, L. Deuker, C. F. Doeller, Mapping sequence structure in the human lateral entorhinal cortex. *eLife* **8**, e45333 (2019). doi: [10.7554/eLife.45333](https://doi.org/10.7554/eLife.45333); pmid: [31383256](https://pubmed.ncbi.nlm.nih.gov/31383256/)
15. S. DuBrow, N. Rouhani, Y. Niv, K. A. Norman, Does mental context drift or shift? *Curr. Opin. Behav. Sci.* **17**, 141–146 (2017). doi: [10.1016/j.cobeha.2017.08.003](https://doi.org/10.1016/j.cobeha.2017.08.003); pmid: [29335678](https://pubmed.ncbi.nlm.nih.gov/29335678/)
16. C. Baldassano et al., Discovering Event Structure in Continuous Narrative Perception and Memory. *Neuron* **95**, 709–721.e5 (2017). doi: [10.1016/j.neuron.2017.06.041](https://doi.org/10.1016/j.neuron.2017.06.041); pmid: [28772125](https://pubmed.ncbi.nlm.nih.gov/28772125/)
17. G. A. Radvansky, J. M. Zacks, Event Boundaries in Memory and Cognition. *Curr. Opin. Behav. Sci.* **17**, 133–140 (2017). doi: [10.1016/j.cobeha.2017.08.006](https://doi.org/10.1016/j.cobeha.2017.08.006); pmid: [29270446](https://pubmed.ncbi.nlm.nih.gov/29270446/)
18. R. G. R. Block, M. A. Reed, M. A., Remembered duration: Evidence for a contextual-change hypothesis. *J. Exp. Psychol. Hum. Learn.* **4**, 656–665 (1978). doi: [10.1037/0278-7393.4.6.656](https://doi.org/10.1037/0278-7393.4.6.656)
19. W. D. Poynter, Duration judgment and the segmentation of experience. *Mem. Cognit.* **11**, 77–82 (1983). doi: [10.3758/BF03197664](https://doi.org/10.3758/BF03197664); pmid: [6855562](https://pubmed.ncbi.nlm.nih.gov/6855562/)
20. Z. Fountas et al., A Predictive Processing Model of Episodic Memory and Time Perception. *Neural Comput.* **34**, 1501–1544 (2022). doi: [10.1162/neco_a_01514](https://doi.org/10.1162/neco_a_01514); pmid: [35671462](https://pubmed.ncbi.nlm.nih.gov/35671462/)
21. J. Zheng et al., Neurons detect cognitive boundaries to structure episodic memories in humans. *Nat. Neurosci.* **25**, 358–368 (2022). doi: [10.1038/s41593-022-01020-w](https://doi.org/10.1038/s41593-022-01020-w); pmid: [35260859](https://pubmed.ncbi.nlm.nih.gov/35260859/)
22. A. Ben-Yakov, Y. Dudai, Constructing realistic engrams: Poststimulus activity of hippocampus and dorsal striatum predicts subsequent episodic memory. *J. Neurosci.* **31**, 9032–9042 (2011). doi: [10.1523/JNEUROSCI.0702-11.2011](https://doi.org/10.1523/JNEUROSCI.0702-11.2011); pmid: [21677186](https://pubmed.ncbi.nlm.nih.gov/21677186/)
23. A. Ben-Yakov, R. N. Henson, The Hippocampal Film Editor: Sensitivity and Specificity to Event Boundaries in Continuous Experience. *J. Neurosci.* **38**, 10057–10068 (2018). doi: [10.1523/JNEUROSCI.0524-18.2018](https://doi.org/10.1523/JNEUROSCI.0524-18.2018); pmid: [30301758](https://pubmed.ncbi.nlm.nih.gov/30301758/)
24. C. Sun, W. Yang, J. Martin, S. Tonegawa, Hippocampal neurons represent events as transferable units of experience. *Nat. Neurosci.* **23**, 651–663 (2020). doi: [10.1038/s41593-020-0614-x](https://doi.org/10.1038/s41593-020-0614-x); pmid: [32251386](https://pubmed.ncbi.nlm.nih.gov/32251386/)
25. N. A. Steinmetz et al., Neuropixels 2.0: A miniaturized high-density probe for stable, long-term brain recordings. *Science* **372**, eabf4588 (2021). doi: [10.1126/science.abf4588](https://doi.org/10.1126/science.abf4588); pmid: [33859006](https://pubmed.ncbi.nlm.nih.gov/33859006/)
26. M. A. Lebedev et al., Analysis of neuronal ensemble activity reveals the pitfalls and shortcomings of rotation dynamics. *Sci. Rep.* **9**, 18978 (2019). doi: [10.1038/s41598-019-54760-4](https://doi.org/10.1038/s41598-019-54760-4); pmid: [31831758](https://pubmed.ncbi.nlm.nih.gov/31831758/)
27. A. De, R. Chaudhuri, Common population codes produce extremely nonlinear neural manifolds. *Proc. Natl. Acad. Sci. U.S.A.* **120**, e2305853120 (2023). doi: [10.1073/pnas.2305853120](https://doi.org/10.1073/pnas.2305853120); pmid: [37733742](https://pubmed.ncbi.nlm.nih.gov/37733742/)

28. S. S. Deshmukh, J. J. Knierim, Representation of non-spatial and spatial information in the lateral entorhinal cortex. *Front. Behav. Neurosci.* **5**, 69 (2011). doi: [10.3389/fnbeh.2011.00069](https://doi.org/10.3389/fnbeh.2011.00069); pmid: [22065409](https://pubmed.ncbi.nlm.nih.gov/22065409/)
29. A. Tsao, M. B. Moser, E. I. Moser, Traces of experience in the lateral entorhinal cortex. *Curr. Biol.* **23**, 399–405 (2013). doi: [10.1016/j.cub.2013.01.036](https://doi.org/10.1016/j.cub.2013.01.036); pmid: [23434282](https://pubmed.ncbi.nlm.nih.gov/23434282/)
30. K. M. Igarashi, L. Lu, L. L. Colgin, M. B. Moser, E. I. Moser, Coordination of entorhinal-hippocampal ensemble activity during associative learning. *Nature* **510**, 143–147 (2014). doi: [10.1038/nature13162](https://doi.org/10.1038/nature13162); pmid: [24739966](https://pubmed.ncbi.nlm.nih.gov/24739966/)
31. I. M. Bright *et al.*, A temporal record of the past with a spectrum of time constants in the monkey entorhinal cortex. *Proc. Natl. Acad. Sci. U.S.A.* **117**, 20274–20283 (2020). doi: [10.1073/pnas.1917197117](https://doi.org/10.1073/pnas.1917197117); pmid: [32747574](https://pubmed.ncbi.nlm.nih.gov/32747574/)
32. A. D. Madar, A. Jiang, C. Dong, M. E. J. Sheffield, Synaptic plasticity rules driving representational shifting in the hippocampus. *Nat. Neurosci.* **28**, 848–860 (2025). doi: [10.1038/s41593-025-01894-6](https://doi.org/10.1038/s41593-025-01894-6); pmid: [40113934](https://pubmed.ncbi.nlm.nih.gov/40113934/)
33. S. N. Chetthi, E. L. Mackevicius, S. Hale, D. Aronov, Barcoding of episodic memories in the hippocampus of a food-caching bird. *Cell* **187**, 1922–1935.e20 (2024). doi: [10.1016/j.cell.2024.02.032](https://doi.org/10.1016/j.cell.2024.02.032); pmid: [38554707](https://pubmed.ncbi.nlm.nih.gov/38554707/)
34. J. G. Heys, D. A. Dombeck, Evidence for a subcircuit in medial entorhinal cortex representing elapsed time during immobility. *Nat. Neurosci.* **21**, 1574–1582 (2018). doi: [10.1038/s41593-018-0252-8](https://doi.org/10.1038/s41593-018-0252-8); pmid: [30349104](https://pubmed.ncbi.nlm.nih.gov/30349104/)
35. W. Yang *et al.*, Selection of experience for memory by hippocampal sharp wave ripples. *Science* **383**, 1478–1483 (2024). doi: [10.1126/science.adk8261](https://doi.org/10.1126/science.adk8261); pmid: [38547293](https://pubmed.ncbi.nlm.nih.gov/38547293/)
36. A. Bragin *et al.*, Gamma (40–100 Hz) oscillation in the hippocampus of the behaving rat. *J. Neurosci.* **15**, 47–60 (1995). doi: [10.1523/JNEUROSCI.15-01-00047.1995](https://doi.org/10.1523/JNEUROSCI.15-01-00047.1995); pmid: [7823151](https://pubmed.ncbi.nlm.nih.gov/7823151/)
37. O. Jensen, L. L. Colgin, Cross-frequency coupling between neuronal oscillations. *Trends Cogn. Sci.* **11**, 267–269 (2007). doi: [10.1016/j.tics.2007.05.003](https://doi.org/10.1016/j.tics.2007.05.003); pmid: [17548233](https://pubmed.ncbi.nlm.nih.gov/17548233/)
38. S. Panzeri, N. Brunel, N. K. Logothetis, C. Kayser, Sensory neural codes using multiplexed temporal scales. *Trends Neurosci.* **33**, 111–120 (2010). doi: [10.1016/j.tins.2009.12.001](https://doi.org/10.1016/j.tins.2009.12.001); pmid: [20045201](https://pubmed.ncbi.nlm.nih.gov/20045201/)
39. D. G. W. Amaral, in *The Rat Nervous System*, G. Paxinos, Ed. (Academic Press, 1995), pp. 443–493.
40. R. D. Burwell, D. G. Amaral, Cortical afferents of the perirhinal, postrhinal, and entorhinal cortices of the rat. *J. Comp. Neurol.* **398**, 179–205 (1998). doi: [10.1002/\(SICI\)1096-9861\(19980824\)398:2<179::AID-CNE3>3.0.CO;2-Y](https://doi.org/10.1002/(SICI)1096-9861(19980824)398:2<179::AID-CNE3>3.0.CO;2-Y); pmid: [9700566](https://pubmed.ncbi.nlm.nih.gov/9700566/)
41. T. Hökfelt, Å. Ljungdahl, K. Fuxe, O. Johansson, Dopamine nerve terminals in the rat limbic cortex: Aspects of the dopamine hypothesis of schizophrenia. *Science* **184**, 177–179 (1974). doi: [10.1126/science.184.4133.177](https://doi.org/10.1126/science.184.4133.177); pmid: [4856104](https://pubmed.ncbi.nlm.nih.gov/4856104/)
42. J. H. Fallon, D. A. Koziell, R. Y. Moore, Catecholamine innervation of the basal forebrain. II. Amygdala, suprarhinal cortex and entorhinal cortex. *J. Comp. Neurol.* **180**, 509–532 (1978). doi: [10.1002/cne.901800308](https://doi.org/10.1002/cne.901800308); pmid: [659673](https://pubmed.ncbi.nlm.nih.gov/659673/)
43. S. Soares, B. V. Atallah, J. J. Paton, Midbrain dopamine neurons control judgment of time. *Science* **354**, 1273–1277 (2016). doi: [10.1126/science.aah5234](https://doi.org/10.1126/science.aah5234); pmid: [27940870](https://pubmed.ncbi.nlm.nih.gov/27940870/)
44. J. Y. Lee *et al.*, Dopamine facilitates associative memory encoding in the entorhinal cortex. *Nature* **598**, 321–326 (2021). doi: [10.1038/s41586-021-03948-8](https://doi.org/10.1038/s41586-021-03948-8); pmid: [34552245](https://pubmed.ncbi.nlm.nih.gov/34552245/)
45. R. U. Muller, J. L. Kubie, The effects of changes in the environment on the spatial firing of hippocampal complex-spike cells. *J. Neurosci.* **7**, 1951–1968 (1987). doi: [10.1523/JNEUROSCI.07-07-01951.1987](https://doi.org/10.1523/JNEUROSCI.07-07-01951.1987); pmid: [3612226](https://pubmed.ncbi.nlm.nih.gov/3612226/)
46. C. B. Alme *et al.*, Place cells in the hippocampus: Eleven maps for eleven rooms. *Proc. Natl. Acad. Sci. U.S.A.* **111**, 18428–18435 (2014). doi: [10.1073/pnas.1421056111](https://doi.org/10.1073/pnas.1421056111); pmid: [25489089](https://pubmed.ncbi.nlm.nih.gov/25489089/)
47. R. J. Gardner *et al.*, Toroidal topology of population activity in grid cells. *Nature* **602**, 123–128 (2022). doi: [10.1038/s41586-021-04268-7](https://doi.org/10.1038/s41586-021-04268-7); pmid: [35022611](https://pubmed.ncbi.nlm.nih.gov/35022611/)
48. M. M. Churchland *et al.*, Neural population dynamics during reaching. *Nature* **487**, 51–56 (2012). doi: [10.1038/nature11129](https://doi.org/10.1038/nature11129); pmid: [22722855](https://pubmed.ncbi.nlm.nih.gov/22722855/)
49. A. A. Russo *et al.*, Motor Cortex Embeds Muscle-like Commands in an Untangled Population Response. *Neuron* **97**, 953–966.e8 (2018). doi: [10.1016/j.neuron.2018.01.004](https://doi.org/10.1016/j.neuron.2018.01.004); pmid: [29398358](https://pubmed.ncbi.nlm.nih.gov/29398358/)
50. B. Kanter, C. Lykken, I. Polti, M.-B. Moser, E. Moser, Electrophysiological recordings from entorhinal cortex and hippocampus in freely behaving adult male rats (v1.0), data set, EBRAINS (2025). doi: [10.25493/GTVB-FQR](https://doi.org/10.25493/GTVB-FQR)
51. B. Kanter, kavli-ntnu/events_Science2025: Inital release, version 1.0.0, Zenodo (2025). doi: [10.5281/zenodo.15199756](https://doi.org/10.5281/zenodo.15199756)

ACKNOWLEDGMENTS

We thank A. M. Amundsgård, S. Ball, K. Haugen, E. H. Holmberg, K. J. Jenssen, E. Kråkvik, and H. Waade for technical assistance; the veterinary staff for animal care; R. Gardner and V. A. Normand for initial training with Neuropixels; and B. A. Dunn, J. A. Gallego, R. Gardner, S. Gonzalo Cogno, A. Lautrup, J. Sugar, A. Z. Vollan, and T. Waaga for discussions. **Funding:** This study was supported by ERC Synergy Grant 951319 (E.I.M.); Research Council of Norway [Centre of Neural Computation 223262 (E.I.M. and M.-B.M.) and Centre for Algorithms in the Cortex 332640 (E.I.M. and M.-B.M.)]; the Kavli Foundation; the Ministry of Science and Education, Norway; the K.G. Jebsen Foundation (grant no. SKGJ-MED-022) (E.I.M. and M.-B.M.); Central Norway Regional Health Authorities (project no. 2020-103253-02-01-04) (E.I.M. and M.-B.M.); and St Olavs Hospital–Trondheim University Hospital (E.I.M. and M.-B.M.). **Author contributions:** E.I.M., M.-B.M., B.R.K., and C.M.L. conceptualized and planned experiments and analyses; B.R.K., C.M.L., and I.P. performed experiments; B.R.K. and I.P. wrote software; B.R.K. and I.P. analyzed data; B.R.K. curated data; B.R.K., C.M.L., and I.P. visualized data; all authors contributed to interpretation; B.R.K. wrote the first draft of the paper; and B.R.K. and E.I.M. edited the paper, with periodic inputs from M.-B.M., C.M.L., and I.P. E.I.M. and M.-B.M. supervised and funded the project. **Competing interests:** The authors declare that they have no competing interests. **Data and materials availability:** All data are available in the manuscript or the supplementary materials or are deposited at EBRAINS (50). Code and preprocessed data files for reproducing the figures are deposited at Zenodo (51). **License information:** Copyright © 2025 the authors, some rights reserved; exclusive licensee American Association for the Advancement of Science. No claim to original US government works. <https://www.science.org/about/science-licenses-journal-article-reuse>

SUPPLEMENTARY MATERIALS

science.org/doi/10.1126/science.adr0927

Figs. S1 to S16; Tables S1 and S2; MDAR Reproducibility Checklist

Submitted 18 June 2024; resubmitted 2 February 2025; accepted 14 April 2025

[10.1126/science.adr0927](https://doi.org/10.1126/science.adr0927)